

University of Twente

EEMCS / Electrical Engineering
Control Engineering



Flexible Needle Steering using Fiber Bragg Grating Sensors

M. (Marco) Kemp

MSc Report

Committee:

Prof. dr. ir. S. Stramigioli
Dr. S. Misra
Prof. dr. ir. H.F.J.M. Koopman
Dr. R. Carloni
M. Abayazid, MSc
R.J. Roesthuis, MSc

August 2012

Report nr. 021CE2012
Robotics and Mechatronics
EE-Math-CS
University of Twente
P.O. Box 217
7500 AE Enschede
The Netherlands

Abstract

Flexible needles with asymmetric (beveled) tips allow steering along curved paths. Such needles can enable diagnosis (e.g., tissue sample removal during biopsies) and treatment (e.g., radioactive seed placement during brachytherapy). Previous research on robotically steering such needles has used clinical imaging modalities as feedback to control the path of the needles. Unfortunately, these imaging modalities have several drawbacks such as low spatial resolution (ultrasound images), low refresh rate (magnetic resonance images) and high doses of radiation (computed tomography scans). As an alternative, sensors that can be embedded in a needle can be used to reconstruct the needle shape to control its path.

Fiber Bragg grating (FBG) sensors are miniaturized optical sensors which can be used to measure strain. Due to their small size (75-250 μm diameter), they can be embedded in flexible needles. By placing several of these sensors along the needle shaft, the curvature can be determined from the measured strains. This is then used to reconstruct the three-dimensional (3D) needle shape. In this study, four sets of three FBG sensors have been embedded in a flexible nitinol needle. The needle shape is reconstructed for both two- and three-dimensional deflections in free space with an average tip position accuracy of 0.9-1.4 mm.

Experiments are also done in soft-tissue phantoms. Needle shape is reconstructed in 3D for both in-plane and out-of-plane insertions in phantoms with an average tip position accuracy of 1.5-2.1 mm. A 3D needle steering controller based on the kinematics-based unicycle model is developed and used to steer the needle to a desired target. Real-time FBG needle shape reconstruction is used as feedback to control the needle path. Obtained steering results show an average targeting error of 1.3 mm.

Acknowledgements

Successfully completing this project would not have been possible without a number of people. First of all I would like to thank my thesis supervisor, Dr. Sarthak Misra for giving me the opportunity to get to know the field of medical robotics and for the meetings and feedback throughout the project. I would also like to thank my daily supervisors Momen Abayazid and Roy Roesthuis for their flexibility, assistance and feedback throughout the project.

During the course of the project numerous other medical robotics group members, the CE secretaries, CE technicians and many others were of great help when I encountered (practical) problems or needed a sounding board. In particular I would like to mention my fellow graduate students Guus Vrooijink and Sander Janssen for assisting me when I was lost in the land of includes, linkers, threads, visual studio, C(++), CANBus, WinPcap and global variables.

Last but not least I would also like to thank my family and especially my father, Bob, and girlfriend, Martine. First of all for proofreading my thesis, but moreover because I can imagine that I might have been preoccupied with my graduation, especially during the last months of the project. Thanks for keeping faith and helping out when I needed it!

–Marco Kemp

Contents

Contents

Introduction	3
Part I: Calibration and Shape Reconstruction of a Flexible Needle using Fiber Bragg Grating Sensors	7
Part II: Real-Time Flexible Needle Steering using Fiber Bragg Grating Sensors	19
Discussion	31
Appendices	33

Introduction

During the last decade, minimally invasive surgery (MIS), has quickly become common practice in medical procedures. An example of MIS is percutaneous surgery, in which the procedure is performed by puncturing the skin using a needle. Percutaneous surgery can sometimes be used as an alternative to traditional open surgery. This reduces the risk of complications (e.g. infection, bleeding) and is less stressful (i.e. faster and less painful recovery) for the patient. Fig. 1a shows an example of percutaneous surgery in which a needle is used for biopsy. Fig. 1b shows an example of percutaneous surgery used for brachytherapy.

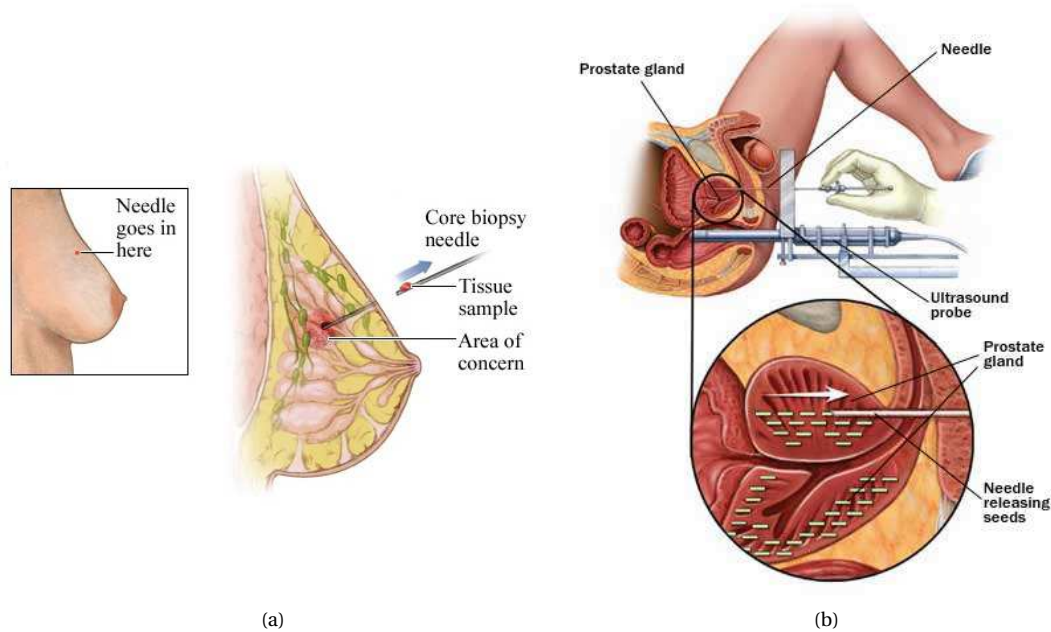


Fig. 1: Examples of minimally invasive percutaneous procedures. (a) Breast biopsy: a needle is used to take a small tissue sample for diagnosis (© Healthwise Incorporated). (b) Prostate Brachytherapy: a needle is used to insert small radioactive seeds into the prostate near a tumor (© Mayo Foundation for Medical Education and Research).

The drawback of a percutaneous procedure is the possibility of an incorrect diagnosis due to targeting errors. Needles used in these procedures have asymmetric (beveled) tips that easily cut and penetrate tissue, and also allow the physician to steer the needle. Despite feedback on the position of the needle and the target, manual needle insertion is still a challenge. Decreasing needle diameter and stiffness allow the needle to follow more curved paths. This can be used to steer the needle towards a target in case of misplacement, or even to avoid sensitive structures between the needle insertion point and the target. This is illustrated in Fig. 2.

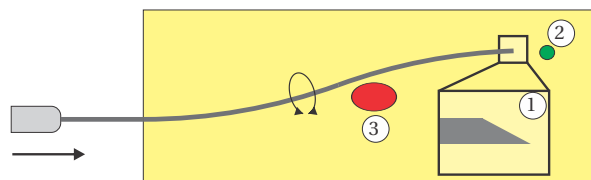


Fig. 2: Schematic illustration showing the insertion of a flexible needle with beveled tip ① into a tissue. A rotation is applied during the insertion to change bending direction and reach the target ② while avoiding an obstacle ③.

As an alternative to manual insertion, a robotic system can be used to insert the needle, taking feedback regarding both needle and target position into account. One can use imaging modalities such as ultrasound (US), x-ray computed tomography (CT) and magnetic resonance imaging (MRI) for visual feedback or use a sensor system which relies on internal sensors within the needle. An example of the latter are Fiber Bragg Grating (FBG) sensors, that allow needle shape reconstruction from strain measurements. An illustration of a Bragg grating is shown in Fig. 3.

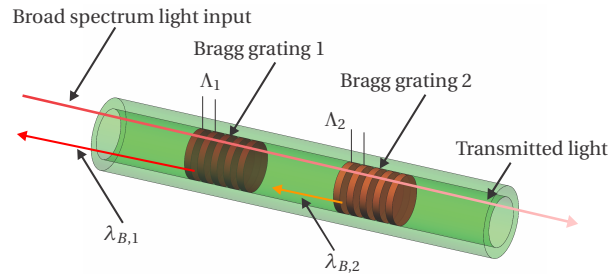


Fig. 3: Two fiber Bragg gratings etched into one fiber, both reflecting a certain wavelength of light ($\lambda_{B,i}$). The wavelength of the reflected light depends on the grating period (Λ_i), which is influenced by strains in the fiber.

Thesis outline

This thesis is composed of two manuscripts. In the first part needle shape reconstruction using FBG sensors is investigated. Experiments are performed for two- and three-dimensional (3D) deflections in air. The second part of this thesis uses the knowledge obtained in the first part to perform 3D needle shape reconstruction in gelatin tissue phantoms. It also shows real-time control and steering of a needle based on the FBG needle shape reconstruction in order to reach a predefined target. This thesis concludes with a reflection on the work done and recommendations for future work.

Part I

'Calibration and Shape Reconstruction
of a Flexible Needle using Fiber Bragg
Grating Sensors'

Calibration and Shape Reconstruction of a Flexible Needle using Fiber Bragg Grating Sensors

Marco Kemp, Momen Abayazid, Roy J. Roesthuis and Sarthak Misra

Abstract—Flexible needles are being researched for medical diagnosis (e.g., biopsies) and therapy (e.g., radioactive seed placement during brachytherapy). Following curved trajectories during needle insertion becomes possible if an asymmetric (beveled) tip is used. Feedback on the needle shape is then required to steer the needle to its target. In the current study, the three-dimensional (3D) configuration of a flexible needle is determined using four sets of three Fiber Bragg Grating (FBG) sensors placed along the length of the needle. FBG locations and needle hysteresis are calibrated using single bend two-dimensional (2D) experiments. Using this calibration, the needle shape is reconstructed in 3D for single and double bend in-plane and out-of-plane deflections. The 3D position of the needle tip was reconstructed with an average error of 1.0 mm for 2D deflections and 1.4 mm for 3D deflections.

Index Terms—Biomedical transducers, Bragg gratings, flexible needle, medical robotics, needle insertion, optical fiber sensors, strain measurement.

I. INTRODUCTION

Needle insertion into soft tissue is one of the most common minimally invasive medical interventions. It is used for both diagnosis (e.g., biopsy) and therapy (e.g., brachytherapy, cryotherapy). Flexible needles with asymmetric (beveled) tips allow the clinician to steer the needle to the desired target along curved trajectories [1]. To do this accurately, it is important for the clinician to receive feedback concerning the deflected shape of the needle. Previous research on needle insertion has focused on using clinical imaging modalities such as ultrasound, x-ray computed tomography (CT) and magnetic resonance imaging (MRI) [1], [2]. However, 3D ultrasound has limited accuracy [3] and the refresh rate for MRI is low for real-time applications [4]. CT is widely used but uses high doses of radiation [5].

As an alternative to external imaging modalities, sensors can be used that can be integrated in the needle. This would provide an accurate shape measurement, without having to use external imaging equipment. Fiber Bragg Grating (FBG) sensors can be integrated into a needle and have recently been used for shape sensing in conventional steel needles [6], [7]. FBG sensors have several advantages such as immunity to electromagnetic interference and high sensitivity. Due to their high sensitivity to strain, FBG sensors can be applied directly to a structure without the need for strain amplifying features. Other advantages of FBG sensors are their small size and the possibility to place multiple sensors in a single fiber. Besides strain, FBG sensors are also sensitive to temperature and have been used in temperature measurement applications [8].

There has been no research to determine the possibilities of FBG sensors in flexible Nitinol needles for 3D shape

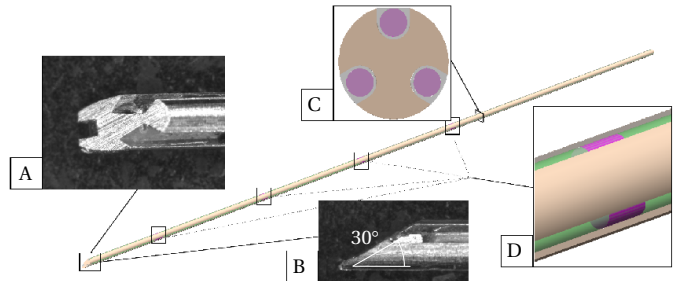


Fig. 1. Illustration of the Nitinol flexible needle showing fiber grooves (A), beveled tip (B), needle cross-section (C) and four fiber Bragg grating sensor locations (D).

reconstruction. The goal of this research is to show that FBG sensors can be used to accurately estimate needle shape. This paper focuses on calibration of a flexible Nitinol needle containing FBG sensors and needle shape reconstruction in free-space when applying one or two deflections to a the needle. An illustration of the needle used in this research is shown in Fig. 1.

In Section II of this study, FBG sensors are explained and the theory to determine the deflected needle shape is discussed. In Section III the setup used in this research is described. In Section IV an overview of the calibration of the needle is given and in Section V the results of the needle shape reconstruction are shown. In Section VI conclusions are drawn and recommendations for future work are made.

II. ANALYSIS OF FBG NEEDLE SHAPE RECONSTRUCTION

The theory behind using FBG sensors to measure strain is described in Section II-A. In Section II-B the method of shape reconstruction using FBG sensors is explained.

A. FBG sensors

The sensors used in this research are based on Bragg gratings. These gratings are etched in a fiber and reflect light according to the changed refractive index of the core and the period at which the grating is applied [9]. The wavelength of the reflected light (λ_B) can be obtained from these properties using

$$\lambda_B = 2n_{eff}\Lambda, \quad (1)$$

where n_{eff} and Λ are the effective refractive index and period of the grating, respectively. An illustration of two FBG sensors in a single fiber is shown in Fig. 2.

By taking partial derivatives of Eq. 1 to temperature (T) and length (l), the change of the reflected light wavelength

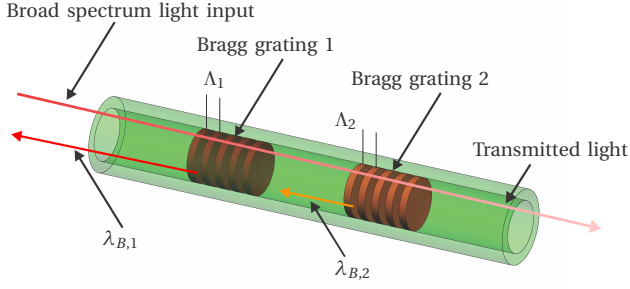


Fig. 2. Illustration showing two fiber Bragg gratings etched into one fiber, both reflecting a certain wavelength of light ($\lambda_{B,1}$ and $\lambda_{B,2}$). The wavelength of the reflected light depends on the effective refractive index of the fiber and the grating period Λ_i for sensor i .

($\Delta\lambda_B$) can be related to the changes in length (Δl) and temperature (ΔT) by [9]

$$\Delta\lambda_B = \underbrace{2 \left[\Lambda \frac{\partial n_{eff}}{\partial l} + n_{eff} \frac{\partial \Lambda}{\partial l} \right] \Delta l}_{\text{Term 1}} + \underbrace{2 \left[\Lambda \frac{\partial n_{eff}}{\partial T} + n_{eff} \frac{\partial \Lambda}{\partial T} \right] \Delta T}_{\text{Term 2}} \quad (2)$$

Term 1 in Eq. 2 represents the effect of the strain (ϵ_z) on the Bragg wavelength and can be rewritten as [9]

$$\Delta\lambda_{B,0} = \lambda_B \left[1 - \frac{n^2}{2} \underbrace{[p_{12} - \nu(p_{11} + p_{12})]}_{P_\epsilon} \right] \epsilon_z, \quad (3)$$

where p_{11} and p_{12} are the strain optic coefficients, n is the refractive index, ν is Poisson's ratio and strain $\epsilon_z = \Delta l/l$. Substituting the photo-elastic coefficient of the optical fiber (P_ϵ) and rewriting Eq. 3 gives

$$\frac{\Delta\lambda_{B,\epsilon}}{\lambda_B} = (1 - P_\epsilon) \epsilon_z. \quad (4)$$

where $\Delta\lambda_{B,\epsilon}$ is the change in Bragg wavelength due to strain.

Term 2 in Eq. 2 represents the change in Bragg wavelength due to temperature change ($\Delta\lambda_{B,T}$) and can be rewritten as [9]

$$\frac{\Delta\lambda_{B,T}}{\lambda_B} = (\alpha_\Lambda + \alpha_n) \Delta T, \quad (5)$$

where ΔT is the temperature change, α_Λ is the thermal expansion coefficient for the fiber and α_n is the thermo-optic coefficient of the fiber. Eq. 1 to 5 show that the wavelength shift of the reflected light has a linear relation with the strain on the FBG and the temperature change of the fiber.

As $\Delta\lambda_B$ is linearly related to the strain (ϵ_z) (Eq. 4), a direct formula for the strain measured by FBG sensor i (ϵ_i) can be given by

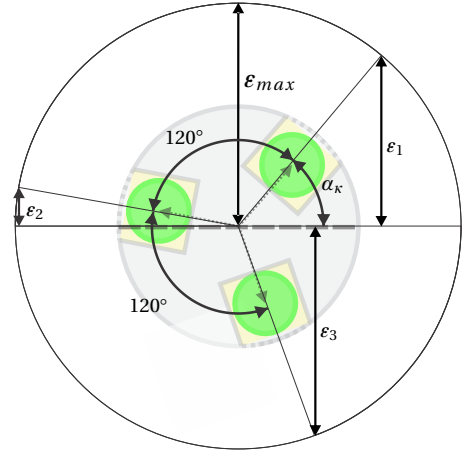


Fig. 3. Cross section of the needle at a measurement location along the needle, showing strain measurements (ϵ_i) corresponding to total strain amplitude (ϵ_{max}) and direction (α_κ)

$$\epsilon_i = \frac{1}{\lambda_B(1 - P_\epsilon)} \Delta\lambda_B + \epsilon_{i,0} + \epsilon_{i,T} \quad (6)$$

where $\epsilon_{i,0}$ is the offset in measured strain due to the base wavelength λ_B and $\epsilon_{i,T}$ is the strain measured due to temperature changes (ΔT) in the FBG sensor.

In order to measure the strain in 3D and also be able to compensate for temperature changes, three sensors need to be placed at each measurement location along the needle. These sensors are placed symmetrically around the needle at 120° angles with respect to each other. This results in three strain measurements per measurement location along the needle's length. Defining the strain in the needle due to bending according to its magnitude (ϵ_{max}) and direction with respect to fiber 1 (α_κ), results in a system according to Fig. 3. The set of equations for the measured strains according to Eq. 6 then becomes:

$$\begin{aligned} \epsilon_1 &= \epsilon_{1,0} + \epsilon_{1,T} + \sin(\alpha_\kappa) \cdot \epsilon_{max} \\ \epsilon_2 &= \epsilon_{2,0} + \epsilon_{2,T} + \sin(\alpha_\kappa + 120^\circ) \cdot \epsilon_{max} \\ \epsilon_3 &= \epsilon_{3,0} + \epsilon_{3,T} + \sin(\alpha_\kappa + 240^\circ) \cdot \epsilon_{max} \end{aligned} \quad (7)$$

where the numerical values for $\epsilon_{i,0}$ can be taken into account during calibration and can thus be assumed zero for further calculations. The temperature dependencies described by $\epsilon_{i,T}$ are assumed equal for the three FBG sensors at a single location along the needle. The set of equations described in Eq. 7 can then be solved to give ϵ_{max} , α_κ and $\epsilon_{i,T}$ for measurement inputs ϵ_1 , ϵ_2 and ϵ_3 :

$$\begin{aligned} \epsilon_{i,T} &= \frac{\epsilon_1 + \epsilon_2 + \epsilon_3}{3} \\ \epsilon_{max} &= -\frac{2}{3} \cdot \sqrt{\epsilon_1^2 + \epsilon_2^2 + \epsilon_3^2 - \epsilon_1 \cdot \epsilon_2 - \epsilon_1 \cdot \epsilon_3 - \epsilon_2 \cdot \epsilon_3} \\ \alpha_\kappa &= 2 \cdot \arctan \left(\frac{3 \cdot \epsilon_{max} + \sqrt{3} \cdot \epsilon_2 - \sqrt{3} \cdot \epsilon_3}{2 \cdot \epsilon_1 - \epsilon_2 - \epsilon_3} \right) \end{aligned} \quad (8)$$

If we assume the needle is a slender beam under pure bending (Fig. 4), the strain due to bending (ϵ_{max}) relates to the curvature (κ) by

$$\epsilon_{max} = \frac{d}{\rho} = d \cdot \kappa, \quad (9)$$

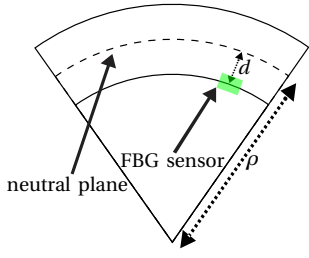


Fig. 4. Schematic representation of beam showing radius of curvature (ρ) and the distance of the sensors to the neutral plane (d)

where d is the distance between the sensors and the neutral plane and ρ is the radius of curvature of the needle at the sensor location.

B. Shape reconstruction

Using Eq. 9, the curvature of the needle can be calculated at the locations of the FBG sensors in the needle. However, to reconstruct the needle shape, the curvature needs to be known at each position along the needle. To obtain a function that describes this curvature, an appropriate curvature function needs to be fitted to the measured curvatures. This study tries to find a fitting function that is suitable for multiple applications: free air deflection and needle insertion into soft tissue. In Section II-B1 the method to obtain an accurate fitting method is described. Section II-B2 describes how needle shape is reconstructed from the curvature. The frame convention used is shown in Fig. 5.

1) *Curvature fitting*: An accurate fitting method is determined for both free-space deflections as well as soft tissue needle insertions. For free-space deflection, beam theory was used to obtain the theoretical curvature from the imposed deflections at locations x_{p1} and x_{p2} (Fig. 6a). According to Misra *et al.* [10] and Webster *et al.* [11], the curvature of a needle in soft tissue can be described using constant curvature sections. As the curvature is expected to be continuous, these constant curvature sections are expected to be interconnected linearly (Fig. 6b).

For this research, the magnitude of curvature for the constant curvature sections was experimentally determined to be $2.5 m^{-1}$ for needle (1 mm diameter) insertions into a 15% gelatin phantom (15% gelatin, 85% water). The part of the needle over which the curvature changes linearly was

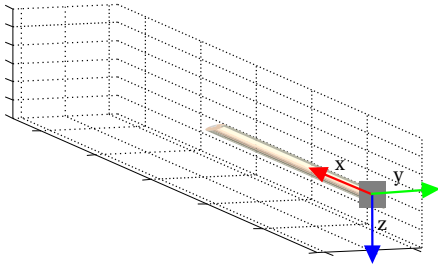


Fig. 5. Frame convention used in needle shape reconstruction

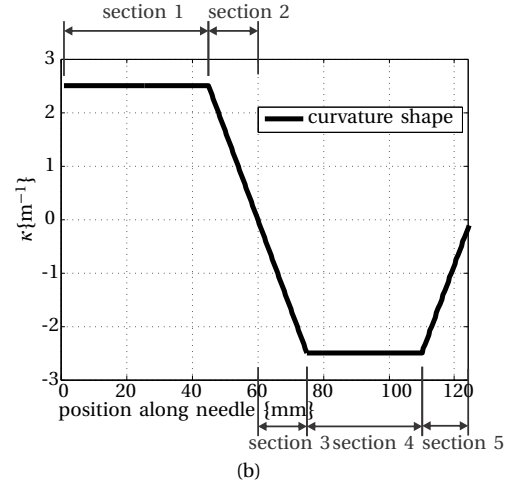
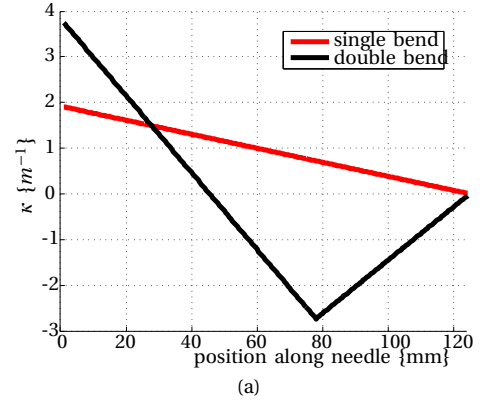


Fig. 6. Examples of theoretical curvatures for: (a) shows single bend and double bend theoretical curvature shapes for free space deflections. (b) shows the assumed theoretical curvature shape for a double bend insertion. Section 1 and 3 are constant curvature sections, sections 3, 4 and 5 are the linear interconnections

also determined during these experiments to be 15 mm for a change from $2.5 m^{-1}$ to $0 m^{-1}$.

An appropriate fitting method can be selected by evaluating the fitted curvature for several fitting functions (Appendix III)[12], [13]:

- A nearest neighbor (NN) interpolation, assuming sections of constant curvature
- A polynomial fit (POLFIT), assuming a continuous curvature function
- A cubic spline (SPLINE), assuming a smooth curvature function
- a Piecewise Cubic Hermite Interpolating Polynomial (PCHIP), combining the properties of a polynomial fitting with reduced overshoot.

The chosen fitting method is applied to the 3D curvature defined according to ϵ_{max} and α_κ . The fitted curvature function is then sampled (samples $k = 1, \dots, n$) at a continuous interval to provide a description of the curvature and its direction ($\kappa[k], \alpha_\kappa[k]$) along the needle.

2) *Integration method*: The interpolated curvature ($\kappa[k], \alpha_\kappa[k]$), as described in Section II-B1, provides a description for the curvature along the entire needle. For small beam deflections and small slope, the relation between the curvature (κ) and needle shape ($y(x)$) reduces

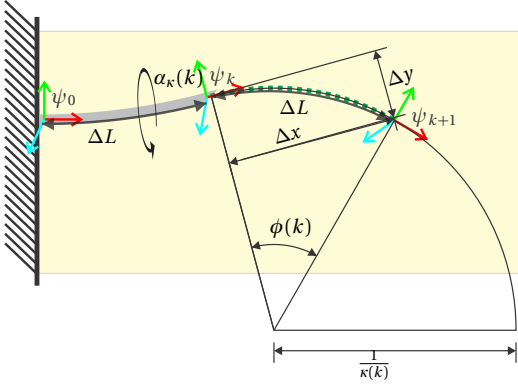


Fig. 7. Illustration of frame based numerical integration method showing displacements Δx and Δy , angle $\phi(k)$, sampling length ΔL and curvature $\kappa(k)$ and its direction $\alpha_{\kappa}(k)$

to the linear beam theory case [14] and is given for 2D by

$$\kappa = \frac{d^2 y(x)}{dx^2}. \quad (10)$$

It is assumed that the slope and deflection at the insertion point of the needle are equal to zero. Therefore by integrating Eq. 10 twice, the equation for the needle shape becomes

$$y(x) = \int_0^x \left(\int_0^x \kappa \cdot dx \right) \cdot dx \quad (11)$$

Shape calculation according to Eq. 10 and 11 is however only valid for small deflections (i.e. $\frac{dy}{dx} < 0.1$ gives less than 1% error). Deflections can often be expected to be larger than 10% of the insertion distance [10]. To eliminate the error caused by using linearized beam theory, a numeric integration method is developed. This integration method takes all slopes and angles into account, by taking a frame based approach. Homogeneous matrices are used to calculate the transformations between the defined frames. (Fig. 7).

$$\mathbf{H}_{k=0}^0 = \begin{bmatrix} 1 & 0 & 0 & 0 \\ 0 & 1 & 0 & 0 \\ 0 & 0 & 1 & 0 \\ 0 & 0 & 0 & 1 \end{bmatrix} \quad (12)$$

$$\mathbf{H}_{k,\alpha_{\kappa}}^k = \begin{bmatrix} \mathbf{R}_{k,\alpha_{\kappa}}^k(-\alpha_{kappa}(i), 0, 0) & 0 \\ 0 & 0 & 0 & 1 \end{bmatrix} \quad (13)$$

$$\phi(k) = \Delta L \cdot \kappa(k) \quad (14)$$

$$\begin{aligned} \Delta x(k) &= \left\| \sin(\phi(k)) \right\| \cdot \frac{1}{\kappa(k)} \\ \Delta y(k) &= (1 - \left\| \cos(\phi(k)) \right\|) \cdot \frac{1}{\kappa(k)} \end{aligned} \quad (15)$$

$$\mathbf{H}_{k+1}^{k,\alpha_{\kappa}} = \begin{bmatrix} \mathbf{R}_{k+1}^{k,\alpha_{\kappa}}(0, -\phi(i), 0) & \Delta x(k) \\ 0 & \Delta y(k) \\ 0 & 0 & 0 & 1 \end{bmatrix} \quad (16)$$

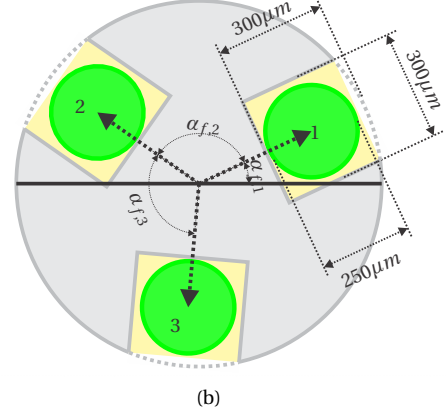
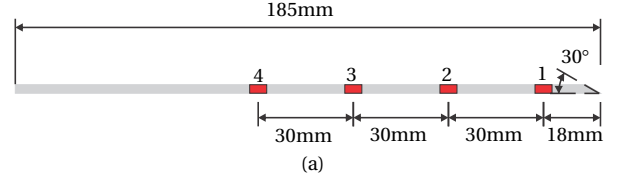


Fig. 8. Schematic representation of needle with FBG locations: (a) shows bevel angle and sensor set locations. (b) shows 1000 μm cross section with three embedded 250 μm diameter fibers in 300 μm deep and wide grooves and the angle of the fibers with respect to each other ($\alpha_{f,i}$), the angle for fiber 1 is defined with respect to the xy plane while the needle is not rotated.

$$\mathbf{H}_{k+1}^0 = \mathbf{H}_k^0 \cdot \mathbf{H}_{k,\alpha_{\kappa}}^k \cdot \mathbf{H}_{k+1}^{k,\alpha_{\kappa}} \cdot (\mathbf{H}_{k,\alpha_{\kappa}}^k)^{-1} \quad (17)$$

First of all, a frame ($\psi_{k=0}$) with zero rotation is defined at the base of the needle (Eq. 12). Next, a frame ($\psi_{k,\alpha_{\kappa}}$) is defined at the same location, rotated according to the direction ($\alpha_{\kappa}(k)$) of the curvature sample at this location (Eq. 13). The translation and rotation are calculated according to the magnitude of the curvature sample ($\kappa(k)$), as visualized in Fig. 7. A new frame (ψ_{k+1}) is defined (Eq. 14 to 16) according to this translation and rotation and the homogeneous matrix relating ψ_{k+1} to ψ_0 is calculated (Eq. 17). For each subsequent curvature sample point k , Eq. 13 to 17 are repeated.

III. SETUP DESIGN

For experiments in this study the FBG needle is used in an experimental setup consisting of a needle insertion stage and two 3D printed plates that can impose a deflection on the needle. These parts are described in this section.

A. FBG needle

The flexible Nitinol needle used in this research has a total length of 185 mm, a maximum insertion length of 150 mm (limited by the setup) and a diameter of 1 mm. FBG sensors are placed at four locations along the needle shaft (Fig. 8a). At each of these locations three FBG sensors are placed in the needle at 120° angles (Fig. 8b). This allows us to measure strain in 3D and compensate for temperature influences on the FBG sensors (Eq. 7).

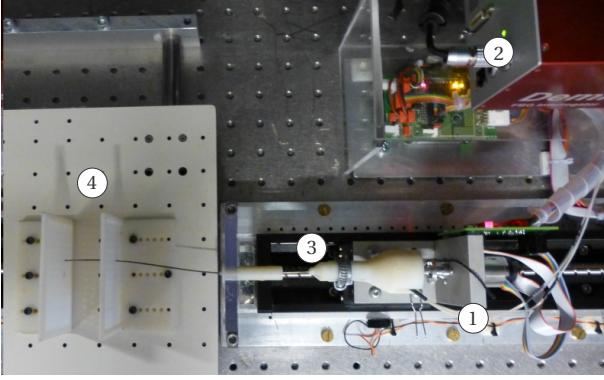


Fig. 9. Experimental setup with fiber Bragg grating (FBG) needle mounted. ① shows the insertion stage with linear drive and rotational motor, ② is the FBG interrogator, ③ is the FBG needle mounted in a three-dimensional (3D) printed holder and ④ shows the two 3D printed plates used to impose deflections on the needle.

To integrate the FBG sensors in the needle, three $300\ \mu\text{m}$ deep grooves are made at 120° angles along the needle using precision milling. Fibers ($250\ \mu\text{m}$ diameter) containing four FBG sensors per fiber, are glued in these grooves using X60 two component adhesive (HBM Germany, Darmstadt, Germany). For precise fiber positioning, markers are made at the FBG locations under a microscope. A 30° bevel tip is made on the needle using a belt sanding machine. The resulting needle is shown in Fig. 1. Theoretical values for sensor locations and measured distances from the needle tip (d_{tip}) are shown in Tab. I.

B. Experimental setup

A setup capable of translation and rotation of the needle is used for needle placement (Fig. 9). This setup consists of a translational stage for insertion, on which a rotational motor is mounted. The needle is mounted on the shaft of this rotational motor. Deflections are applied to the needle to validate the FBG needle shape reconstruction. Two plates are 3D printed with 1.5 mm hole grids at 5 mm spacing. The plates allow imposed deflections ranging from -30 mm to +30 mm in y-direction and -30 mm to 20 mm in z-direction. The plates are attached to the setup at desired distances from the base of the needle. The needle is then positioned in the desired deflection holes allowing for single bend (one applied deflection) and double bend (two applied deflections) shapes.

Tab. I

THEORETICAL FIBER BRAGG GRATING SENSOR LOCATIONS: $\alpha_{f,i}$ DEFINED AS SHOWN IN FIG. 8B, THE THEORETICAL d (d_{th}) AS USED IN EQ. 9 AND d_{tip} AS THE DISTANCE FROM THE NEEDLE TIP AS SHOWN FOR ALL LOCATION (LOC.) IN FIG. 8

fiber	1	2	3		
loc.	$\alpha_{f,1}\{^\circ\}$	$\alpha_{f,2}\{^\circ\}$	$\alpha_{f,3}\{^\circ\}$	$d_{th}\{\text{mm}\}$	$d_{tip}\{\text{mm}\}$
1	0	120	120	0.35	18
2	0	120	120	0.35	48
3	0	120	120	0.35	78
4	0	120	120	0.35	108

IV. FBG NEEDLE CALIBRATION

As shown in Section III-A, there are several parameters of the needle that need to be calibrated. The values for $\alpha_{f,i}$ and d , as mentioned in Tab. I, need to be determined for each sensor in order to get an accurate measurement of the 3D-strain and -curvature. Besides this, a calibration is needed for the parameters used in Eq. 6 to get accurate strain measurements from each of the twelve sensors. Furthermore, the needle has torsional compliance (Appendix I), which will have an influence during rotation of the needle. This effect can be compensated, based on calibration of the hysteresis during rotation. In Section IV-A the relation between the output of the sensors and the measured strain is characterized. Section IV-B describes the calibration of the distances d between the sensors and the center of the needle and Section IV-C shows the calibration of the angles $\alpha_{f,i}$ and the hysteresis during rotation.

A. FBG sensor calibration

The FBG sensors are combined with the Deminsys Python 850-55 FBG interrogator (Technobis Fiber Technologies BV, Uitgeest, Netherlands). The used interrogator measures the wavelengths reflected by the FBG sensors by projecting the reflected light on a 256 pixel CCD camera display via an optical system. This system uses a dual weighted averaging algorithm to estimate the peak intensity pixel P at 1/1000 pixel accuracy which corresponds to approximately $3\ \mu\epsilon$ sensitivity. The measured peak intensity pixel has a relation with the measured strain ϵ_i [15], [16] for the FBG sensor according to

$$\epsilon_i = \frac{P + C_p}{A \cdot (P + C_p) + B} + \epsilon_{off} \quad (18)$$

in which P is the measured pixel value, with estimated sub-pixel value. C_p depends only on the subpixel value and provides a correction for the assumed linear relation between pixel value and strain. A , B and C_p are determined by applying a sequence of known strains to a fiber equal to the fiber used in the needle while measuring P . Using a linear regression algorithm the values for A and B are determined from the results from this experiment. The values for C_p are determined from the error between P and the result of the linearized fit using A and B [15]. As calibration values are different for each of the three channels of the interrogator that will be used for the three fibers containing FBG sensors, A , B and C_p are determined for for all three of them.

The offset (ϵ_{off}) is determined in the test setup for each FBG sensor. This is done by placing the needle in a straight configuration. The output values for ϵ_i are used as calibration values ϵ_{off} . This offset contains the base wavelength of the specific sensor as well as the room temperature influence on the wavelength.

B. Sensor location calibration

The FBG sensors have been manually glued in the milled grooves in the Nitinol needle. As the distance of the sensor

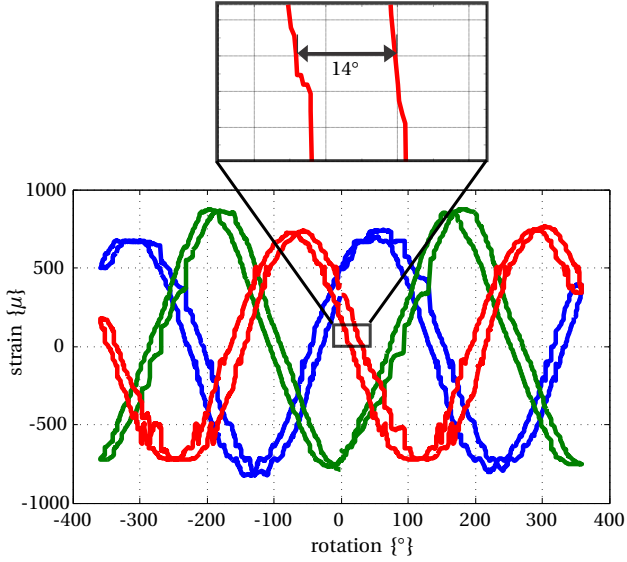


Fig. 10. Measured strains for the three sensors at one sensor set location during a full 360° needle rotation in positive and negative direction and back to the original rotation. Zoomed in section of the measured strain by fiber 1 shows a hysteresis of 14°.

to the center of the needle (d) scales linearly with the strain (Eq. 9) it is important to get an accurate calibration of the distance d for each sensor.

This distance is calibrated by applying a predefined deflection on the needle. The theoretical curvature along the needle is known according to beam theory (Fig. 6a). The theoretical strain (ϵ_{th}) can be determined according to Eq. 9 using the theoretical distance (d_{th}) from Tab. I. While keeping the needle in a constant deflected configuration, it is rotated at 30°/s for a full 360° rotation in both positive and negative direction and back to the original rotation. This results in the measured strains at a single sensor location as shown in Fig. 10. As the expected shape is according to Eq. 7, a sine function has been fitted to the signals from each sensor (Appendix III). The amplitude of this fitted sine (A_{sf}) gives us the actual distance (d) for each sensor according to $d = \frac{A_{sf}}{\epsilon_{th}} \cdot d_{th}$. This experiment is repeated for six tip deflections ([-30;-20;-10;10;20;30] mm), giving a mean d and its standard deviation. The resulting calibration values are shown in Tab. II.

C. Sensor angle and hysteresis calibration

For accurate reconstruction of ϵ_{max} and its direction (α_κ), knowledge about the angles $\alpha_{f,i}$ at which each sensor is

Tab. II

CALIBRATED SENSOR LOCATIONS FROM THE CENTER OF THE NEEDLE (d) WITH STANDARD DEVIATIONS (σ) AND DISTANCES d_{tip} FROM THE TIP OF THE NEEDLE

fiber	1	2	3	
loc.	$d\{\text{mm}\}$	$d\{\text{mm}\}$	$d\{\text{mm}\}$	$d_{tip}\{\text{mm}\}$
1	0.44($\sigma=0.04$)	0.33($\sigma=0.06$)	0.34($\sigma=0.07$)	18
2	0.38($\sigma=0.03$)	0.30($\sigma=0.03$)	0.32($\sigma=0.03$)	48
3	0.40($\sigma=0.02$)	0.31($\sigma=0.03$)	0.30($\sigma=0.02$)	78
4	0.36($\sigma=0.02$)	0.31($\sigma=0.02$)	0.27($\sigma=0.02$)	108

located is important. To determine these angles, the data from the experiments described in Section IV-B can be used. This time the shift of the fitted sine waves provides the information. If the position of the sensors is according to Tab. I, mutual angle shifts should be 120°. The real rotations are shown in Tab. III.

From the same experiments, the hysteresis due to torsion is obtained (Fig. 10). From the set of calibration experiments an average hysteresis (α_{hys}) is determined for each sensor location (Tab. III). During a rotation hysteresis can be compensated, by adding or subtracting half of the hysteresis angle from the direction of the total strain (α_κ) as calculated using Eq. 8.

Using the calibration, and knowledge about the experimental setup, the calculation of the direction of the total strain is changed from Eq. 8 to

$$\alpha_\kappa = 2 \cdot \arctan \left(\frac{3 \cdot \epsilon_{max} + \sqrt{3} \cdot \epsilon_2 - \sqrt{3} \cdot \epsilon_3}{2 \cdot \epsilon_1 - \epsilon_2 - \epsilon_3} \right) + \alpha_{f,1} + \alpha_{enc} \pm \frac{\alpha_{hys}}{2} \quad (19)$$

in which $\alpha_{f,1}$ is given for each sensorset in Tab. III and α_{enc} is the angle at which the entire needle is rotated in the experimental setup by the rotation stage.

V. SHAPE RECONSTRUCTION RESULTS

FBG sensors are used to reconstruct the needle shape using the algorithm described in Section II-B and the calibrated values given in Section IV. The best curvature fitting method is determined by sampling the needle curvature described in Section II-B1 and calculating the resulting shape. For each of the four fitting methods, the theoretical needle shape error (ϵ_{ths}) and tip error (ϵ_{tht}) are determined using the needle shape resulting from the theoretical curvature ($P_{th}(i)$) and the shape resulting from the fitting ($P_{fit}(i)$) according to

$$\epsilon_{ths} = \frac{1}{i} \cdot \sum_{i=1}^{end} \|P_{th}(i) - P_{fit}(i)\| \quad (20)$$

$$\epsilon_{tht} = \|P_{th}(end) - P_{fit}(end)\| \quad (21)$$

The resulting average errors are shown in Tab. IV. These errors show that, theoretically, PCHIP interpolation gives the best results for free-space deflections and NN interpolation gives the best results for soft tissue insertions.

To show that needle shape can be reconstructed using FBG sensors, several experiments are done using the setup

Tab. III

CALIBRATED SENSOR ROTATIONS ($\alpha_{f,i}$) (FIG. 8B) WITH STANDARD DEVIATIONS (σ). AVERAGE HYSTERESIS (α_{hys}) WITH STANDARD DEVIATION (σ) PER SENSOR LOCATION IS ALSO SHOWN.

fiber	1	2	3		
loc.	$\alpha_{f,1}\{\text{°}\}$	$\alpha_{f,2}\{\text{°}\}$	$\alpha_{f,3}\{\text{°}\}$	$\alpha_{hys}\{\text{°}\}$	$d_{tip}\{\text{mm}\}$
1	324($\sigma=7$)	110($\sigma=14$)	124($\sigma=12$)	18($\sigma=8$)	18
2	320($\sigma=2$)	119($\sigma=1$)	122($\sigma=3$)	14($\sigma=4$)	48
3	315($\sigma=4$)	124($\sigma=1$)	118($\sigma=2$)	13($\sigma=3$)	78
4	312($\sigma=5$)	126($\sigma=14$)	114($\sigma=1$)	10($\sigma=3$)	108

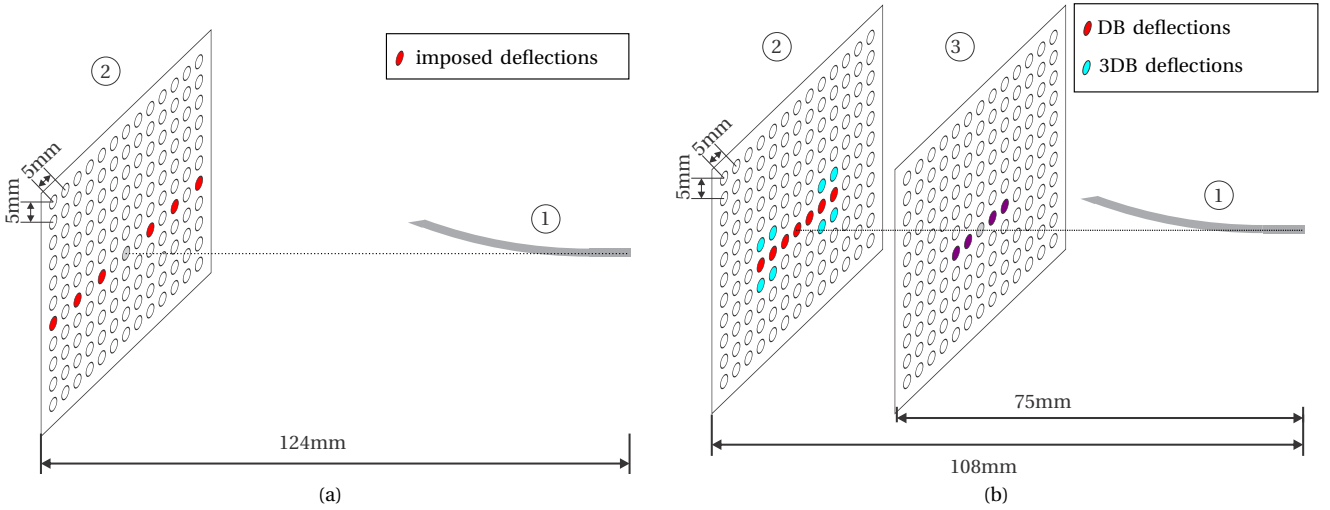


Fig. 11. Figures (a) and (b) show the deflections imposed on the needle ① during shape reconstruction experiments. (a) shows imposed single bend deflections using a single plate ②, (b) shows imposed in-plane and out-of-plane double bend deflections using an extra plate ③.

described in Section III. In-plane single and double bend deflections are applied as well as out-of-plane double bend deflections (Fig. 11). The 3D-printed plates are positioned at 75 mm and 109 mm from the needle base. The total insertion length of the needle is ~110 mm to make sure a sensor measurement is present close to the base (Appendix I). The needle shapes are reconstructed using both NN and PCHIP interpolation (Appendix III). During an applied deflection, the needle is rotated around its length axis for a full 360° rotation in positive and negative direction and back to the original rotation. At 15° intervals the needle shape is determined. In Fig. 12 the resulting average needle shape and standard deviation are shown for each type of deflection.

To determine the accuracy, the difference between the estimated position ($P_{FBG}(x_{ref})$) and imposed deflection (P_{ref}) is determined. The tip error (ϵ_{tip}) is determined for each experiment according to

$$\epsilon_{tip} = \frac{1}{m} \cdot \sum_{\alpha_{enc}} \|P_{ref} - P_{FBG}(\alpha_{enc}, x_{ref})\|. \quad (22)$$

with α_{enc} equal to the needle rotation at 15° sample intervals during the applied full rotations and m equal to the number of samples. The needle shape spread (Fig. 12) is determined separately for each experiment according to

$$\sigma_{spr} = \sigma(P_{ref} - P_{FBG}(\alpha_{enc}, x_{ref})). \quad (23)$$

Tab. IV

AVERAGE THEORETICAL SHAPE RECONSTRUCTION ERRORS FOR THE DIFFERENT INTERPOLATION METHODS

	Free-space		Soft tissue	
	ϵ_{ths} {mm}	ϵ_{tht} {mm}	ϵ_{ths} {mm}	ϵ_{tht} {mm}
NN	0.7	1.5	0.1	0.1
POLFIT	0.7	1.4	0.6	1.3
SPLINE	0.6	1.1	0.5	0.9
PCHIP	0.2	0.3	0.2	0.3

The average tip error and its standard deviation ($\sigma(\epsilon_{tip})$) are calculated for the set of single bend experiments and the set of double bend experiments. Also the minimum and maximum spread are determined for the two sets. Accuracies are calculated using both the NN interpolation as well as the PCHIP interpolation (Tab. V).

Resulting accuracies (Tab. V) show that the NN interpolation produces 2% more accurate results than the PCHIP interpolation, contrary to expectations (Tab. IV). It shows that needle shape can be reconstructed for both single, double and 3D double bend shapes with average tip errors of 0.9 mm, 1.0 mm and 1.4 mm, respectively.

VI. CONCLUSIONS AND RECOMMENDATIONS

This study showed that the shape of a flexible needle can be reconstructed using FBG sensors. A needle containing FBG sensors was calibrated. The torsional compliance in the current needle causes a hysteresis effect when rotating the needle in an environment with friction. The hysteresis was calibrated and hence could be compensated. Needle shape was reconstructed in free-space with a 0.9 mm average tip-error for single bend experiments. Double bend experiments showed a 1.0 mm average 3D tip-error and

Tab. V

NEEDLE SHAPE RECONSTRUCTION ACCURACIES FOR SINGLE BEND (SB), DOUBLE BEND (DB) AND THREE-DIMENSIONAL DOUBLE BEND (3DB) EXPERIMENTS IN FREE-SPACE: AVERAGE TIP ERROR $\mu(\epsilon_{tip})$, TIP ERROR STANDARD DEVIATION $\sigma(\epsilon_{tip})$ AND MIN./MAX. SPREAD $min(\sigma_{spr})$ AND $max(\sigma_{spr})$ ARE SHOWN FOR BOTH NEAREST NEIGHBOR (NN) AND PCHIP INTERPOLATION. ALL VALUES IN THE TABLE ARE IN {MM}.

Shape	Method	$\mu(\epsilon_{tip})$	$\sigma(\epsilon_{tip})$	$min: max(\sigma_{spr})$
SB	NN	0.9	0.5	1.0 : 2.1
	PCHIP	1.0	0.5	1.0 : 2.1
DB	NN	1.0	0.5	1.6 : 3.3
	PCHIP	1.0	0.6	1.6 : 3.3
3DB	NN	1.4	0.6	2.0 : 2.9
	PCHIP	1.4	0.6	2.0 : 2.9

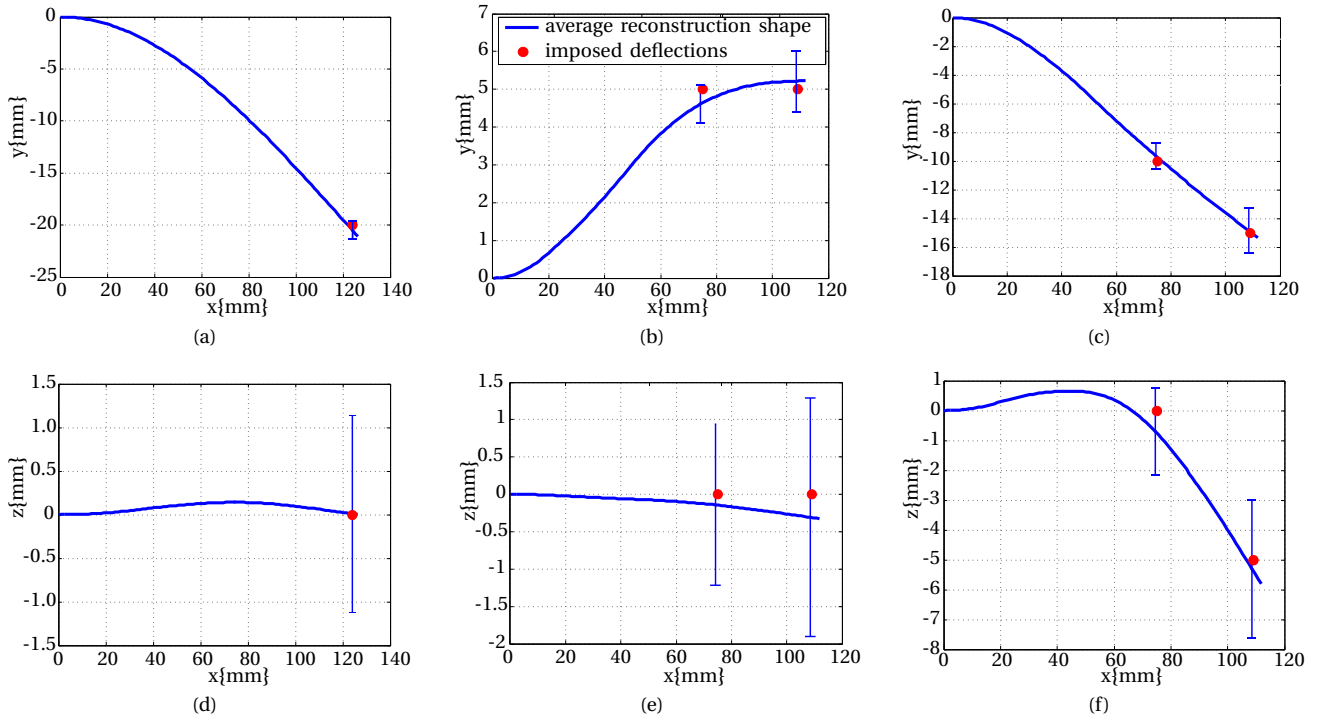


Fig. 12. Needle shape reconstruction examples using nearest neighbor interpolation. (a,d) show a single bend shape, (b,e) show a double bend shape and (c,f) show a 3D double bend shape. Error bars at the tip of the needle indicate the spread (σ_{spr}) of the measurement.

3D double bend shapes were reconstructed with 1.4 mm average tip-error.

Furthermore this study showed that in theory a PCHIP interpolation method is most suitable to reconstruct needle shape when imposing deflections in free-space. However, in practice results from the computationally simpler NN interpolation method were 2% more accurate than the results from the PCHIP interpolation. As a NN interpolation is also expected to give more accurate results for soft tissue insertions, this method is preferable over the PCHIP interpolation.

This study illustrates three needle characteristics that currently limit the accuracy of the needle shape reconstruction. The current needle has torsional compliance, causing hysteresis when rotating the needle. Also, the sensors are located far from the base and their distance to the center of the needle is not accurately known. This reduces the maximum insertion length, as a sensor is needed close to the base of the insertion. Also uncertainties in the location of sensors, due to inaccuracies during fabrication of the needle, cause a spread on the measured needle tip position.

For a future version of the FBG needle, it is recommended to change the design to solve these problems. This could be done by adding more sensors, especially near the needle base. Reducing torsion in the needle will also increase accuracy. This could be done by adding an outer sleeve over the needle. In this way, the needle surface would be smooth, reducing friction. The needle would also be more torsion stiff, reducing torsion due to the remaining friction. Besides this, increasing the control over production steps should increase the accuracy of the theoretical sensor locations and

could even eliminate the need for an elaborate calibration routine. A possibility would be to use multicore fibers, which would decrease the influence of manual production steps on sensor locations.

Theoretically, the FBG sensors and NN interpolation method are also capable of needle shape reconstruction for soft tissue insertions. Investigating if this is indeed possible, what the accuracy is in soft tissue and using the FBG needle shape as a feedback signal for needle control would be very interesting.

ACKNOWLEDGEMENTS

The authors are affiliated with MIRA – Institute for Biomedical Technology and Technical Medicine, University of Twente, The Netherlands. This research is supported by the Dutch Technology Foundation STW, which is part of the Netherlands Organisation for Scientific Research (NWO) and partly funded by the Ministry of Economic Affairs, Agriculture and Innovation.

REFERENCES

- [1] N. Abolhassani, R. Patel, and M. Moallem, "Needle insertion into soft tissue: A survey," *Medical Engineering & Physics*, vol. 29, no. 4, pp. 413 – 431, 2007.
- [2] S. Patil and R. Alterovitz, "Interactive motion planning for steerable needles in 3d environments with obstacles," in *proceeding of the IEEE RAS and EMBS International Conference on Biomedical Robotics and Biomechatronics (BioRob)*, pp. 893 –899, Tokyo, Japan, September 2010.
- [3] P. M. Novotny, J. A. Stoll, N. V. Vasilyev, P. J. del Nido, P. E. Dupont, T. E. Zickler, and R. D. Howe, "Gpu based real-time instrument tracking with three-dimensional ultrasound," *Medical Image Analysis*, vol. 11, no. 5, pp. 458 – 464, 2007.

- [4] S. DiMaio, E. Samset, G. Fischer, I. Iordachita, G. Fichtinger, F. Jolesz, and C. Tempny, "Dynamic mri scan plane control for passive tracking of instruments and devices," in *Medical Image Computing and Computer-Assisted Intervention*, pp. 50–58, Springer Berlin / Heidelberg, 2007.
- [5] H. Fred, "Drawbacks and limitations of computed tomography," *Texas Heart Institute Journal*, vol. 31, no. 2, pp. 345–348, 2004.
- [6] Y.-L. Park, S. Elayaperumal, B. Daniel, C. R. Seok, S. Mihye, J. Savall, R. Black, B. Moslehi, and M. Cutkosky, "Real-time estimation of 3-d needle shape and deflection for mri-guided interventions," *IEEE/ASME Transactions on Mechatronics*, vol. 15, no. 6, pp. 906 – 915, 2010.
- [7] K. Henken, D. Van Gerwen, J. Dankelman, and J. Van Den Dobbelsteen, "Accuracy of needle position measurements using fiber bragg gratings," *Minimally Invasive Therapy & Allied Technologies*, vol. 0, no. 0, pp. 1–7, 2012.
- [8] V. Mishra, N. Singh, U. Tiwari, and P. Kapur, "Fiber grating sensors in medicine: Current and emerging applications," *Sensors and Actuators A: Physical*, vol. 167, no. 2, pp. 279 – 290, 2011.
- [9] A. Othonos, K. Kalli, D. Pureur, and A. Mugnier, "Fibre bragg gratings," in *Wavelength Filters in Fibre Optics*, pp. 189–269, Springer Berlin / Heidelberg, 2006.
- [10] S. Misra, K. Reed, B. Schafer, K. Ramesh, and A. Okamura, "Mechanics of flexible needles robotically steered through soft tissue," *The International Journal of Robotics Research*, vol. 29, no. 13, pp. 1640–1660, 2010.
- [11] R. J. Webster, J. S. Kim, N. J. Cowan, G. S. Chirikjian, and A. M. Okamura, "Nonholonomic modeling of needle steering," *The International Journal of Robotics Research*, vol. 25, no. 5-6, pp. 509–525, 2006.
- [12] C. de Boor, *A Practical Guide to Splines*. Springer-Verlag, 1978.
- [13] MATLAB, "interp1 - 1-d data interpolation."
- [14] T. Megson, *Structural and Stress Analysis*. Butterworth-Heinemann, 2005.
- [15] "Technobis deminsys, calibration procedure," 2012.
- [16] "Technobis deminsys software manual - user manual addition," 2012.

Part II

'Real-Time Flexible Needle Steering
using Fiber Bragg Grating Sensors'

Real-Time Flexible Needle Steering using Fiber Bragg Grating Sensors

Marco Kemp, Momen Abayazid, Roy J. Roesthuis and Sarthak Misra

Abstract—Flexible needles with asymmetric (beveled) tips allow steering along curved paths. Such needles can be used for diagnosis (e.g., tissue sample removal during biopsies) and treatment (e.g., brachytherapy, cryotherapy). Previous research on robotically steering such needles has used clinical imaging modalities as feedback to control the path of the needles. Unfortunately, these imaging modalities have several drawbacks such as low spatial resolution (ultrasound images), low refresh rate (magnetic resonance images) and high doses of radiation (computed tomography scans). As an alternative feedback modality, sensors that can be embedded in a needle can be used to reconstruct the three-dimensional (3D) needle shape. In this study, fiber Bragg grating (FBG) sensors are embedded in a flexible Nitinol needle. Needle shape is reconstructed for both in-plane and out-of-plane needle insertions in soft tissue phantoms with an average tip position accuracy of 1.5-2.1 mm. A 3D needle steering controller based on the kinematics-based unicycle model is developed and used to steer the needle to a desired target. Real-time FBG needle shape reconstruction is used as feedback to control the needle path. Results show an average targeting error of 1.3 mm for 3D target locations.

Index Terms—Biomedical transducers, Bragg gratings, flexible needle, medical robotics, needle steering, optical fiber sensors, strain measurement.

I. INTRODUCTION

Flexible needles with asymmetric (beveled) tips allow steering of the needle along curved paths [1]. Such needles can be used for diagnostic procedures (e.g., tissue sample removal during biopsies) and therapy (e.g., brachytherapy, cryotherapy). Robotically steering such needles has relied on feedback of the needle shape based on clinical imaging modalities such as ultrasound, x-ray computed tomography (CT) and magnetic resonance imaging (MRI) [1], [2]. However, the spatial resolution of three-dimensional (3D) is limited [3] and the use of MRI also has disadvantages (e.g., low refresh rate, incompatibility with magnetic materials)[4]. CT can be used for real-time applications, but exposes the patient to high doses of radiation [5].

Fiber Bragg grating (FBG) sensors are optical sensors that can measure strain [6]. Needle shape reconstruction using FBG sensors has been demonstrated in steel needles [7], [8] and Nitinol needles [9] for single bend and double bend deflections in free-space. Needle path planning and steering of flexible needles have been studied in previous research [2], [10], [11], [12], [13], [14], [15]. When steering these needles along curved trajectories in tissue, real-time needle shape sensing is important. No research has been published on reconstructing 3D needle shape in soft tissue phantoms using FBG sensors in real-time. The combination of FBG-based needle shape feedback for needle insertion control has also not been shown.

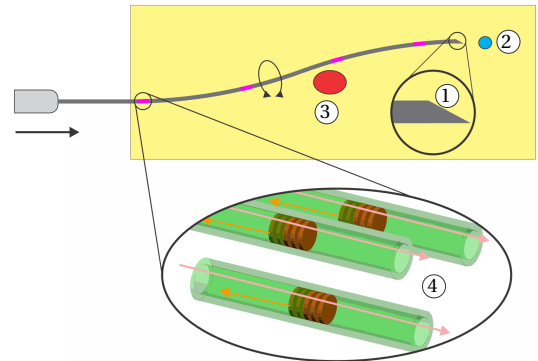


Fig. 1. A needle with beveled tip ① is inserted into a gelatin tissue phantom towards a target ② while an obstacle ③ is avoided. During the insertion, the needle shape is calculated using signals from sets of three fiber Bragg grating sensors ④ positioned along the needle.

The goal of this study, is to demonstrate that a flexible Nitinol needle can be steered inside a gelatin phantom using FBG sensors for real-time needle shape feedback. Using this feedback, the needle is steered toward a target location inside a gelatin phantom (Fig. 1). Section II discusses the theory behind FBG needle shape reconstruction and the needle steering algorithm. In Section III the experimental setup and software are discussed. Section IV shows the results obtained by shape reconstruction in gelatin phantoms and the results of the FBG shape reconstruction combined with the proposed controller. Finally, the conclusions and recommendations for future work are given in Section V.

II. ANALYSIS

Needle shape reconstruction using FBG sensors is described in Section II-A. In Section II-B the needle steering algorithm used to control the needle to a specified target is described.

A. FBG based needle shape reconstruction

In this study, 3D needle shape is reconstructed using FBG sensors (Fig. 2). FBG sensors are based on Bragg gratings and reflect a certain wavelength of light (λ_B). When a strain is applied to these sensors, this wavelength shifts. The relation between the strain (ϵ_i) and wavelength shift ($\Delta\lambda_B$) is given by

$$\epsilon_i = \frac{1}{\lambda_B(1 - P_\epsilon)} \Delta\lambda_B + \epsilon_{T,C} \quad (1)$$

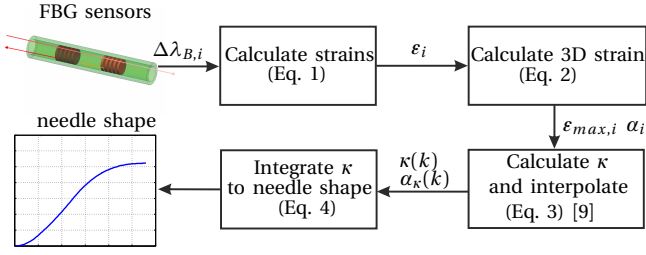


Fig. 2. Flowchart indicating steps in needle shape reconstruction using fiber Bragg grating (FBG) sensors. Strains are calculated according to the wavelength shifts ($\Delta\lambda_i$) measured by the FBG sensors ($i=1,..12$). The three-dimensional (3D) strain ($(\epsilon_{max,n}, \alpha_{\kappa,n})$, $n=1,..4$) is interpolated and sampled (samples k) resulting in a curvature function ($\kappa_k(k), \alpha_{\kappa}(k)$). By double integration of this function, the 3D needle shape is determined.

in which $\epsilon_{T,C}$ is the offset in the measured strain (ϵ_i) due to temperature and Bragg wavelength (λ_B) and P_ϵ is the photo-elastic coefficient of the optical fiber [6], [9].

For our needle, three sensors are placed at each sensor location along the needle. The cross section of the needle at a sensor location is shown in Fig. 3. This configuration allows us to determine the magnitude of the bending strain (ϵ_{max}) and its direction (α_κ) according to

$$\begin{aligned} \epsilon_{max} &= -\frac{2}{3} \cdot \sqrt{\epsilon_1^2 + \epsilon_2^2 + \epsilon_3^2 - \epsilon_1 \cdot \epsilon_2 - \epsilon_1 \cdot \epsilon_3 - \epsilon_2 \cdot \epsilon_3} \\ \alpha_\kappa &= 2 \cdot \arctan\left(\frac{3 \cdot \epsilon_{max} + \sqrt{3} \cdot \epsilon_2 - \sqrt{3} \cdot \epsilon_3}{2 \cdot \epsilon_1 - \epsilon_2 - \epsilon_3}\right) + \alpha_{enc} \pm \frac{\alpha_{hys}}{2} \end{aligned} \quad (2)$$

where ϵ_1 , ϵ_2 and ϵ_3 are the strains measured by the three sensors at a single location, α_{enc} is the rotation of the base of the needle by an experimental setup and α_{hys} is a compensation for hysteresis according to the direction of the rotation [9].

If we assume the needle is a slender beam under pure bending (Fig. 4), the strain due to bending (ϵ_{max}) relates to the curvature (κ) by

$$\epsilon_{max} = \frac{d}{\rho} = d \cdot \kappa \quad (3)$$

in which d is the distance between the sensor and the neutral plane and ρ is the radius of curvature of the needle

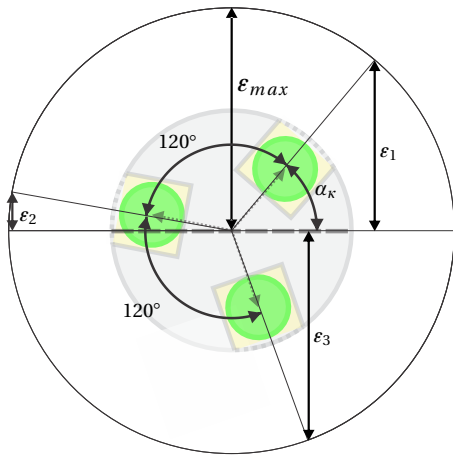


Fig. 3. Schematic overview of the three strain measurements (ϵ_1 , ϵ_2 , ϵ_3) at a sensor set location corresponding to the bending strain in the needle (magnitude ϵ_{max} , direction α_κ)

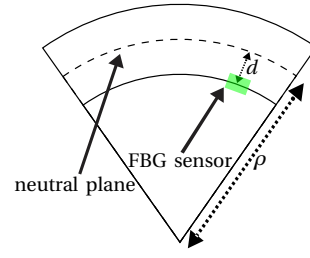


Fig. 4. Schematic representation of beam showing radius of curvature (ρ) and the distance of the sensors to the neutral plane (d)

at the sensor location.

The curvature is only measured at sensor locations and hence interpolation is used to generate the complete curvature function. Sampling (samples k) this function gives a description of the curvature along the needle ($\kappa(k), \alpha_\kappa(k)$). Kemp *et al.* have shown that a nearest neighbor interpolation is in theory an accurate interpolation method needle insertions into a gelatin phantom [9]. For small needle deflections, the curvature can be integrated to obtain the 3D needle shape [16] according to

$$y(x) = \int_0^x \left(\int_0^x \kappa \cdot dx \right) \cdot dx \quad (4)$$

The axis convention used in this study is shown in Fig. 5.

B. Needle steering and control

Needle shape feedback can be used as feedback for the needle steering controller. Besides feedback, the controller predicts the needle path. According to previous research, the needle path can be described by sections of constant curvature [17], [18]. The controller in this study uses this property by predicting the needle path using the expected constant curvature. The direction is predicted using the bevel orientation. The reachable area (R_r) at a certain distance x (in needle tip frame (Ψ_{tip}) (Fig. 7)) can be described by a circle with radius r_{reach} according to

$$r_{reach}(x) = r_\kappa - \sqrt{r_\kappa^2 - x^2} \quad (5)$$

in which r_κ is the expected radius of curvature the needle will travel along (Fig. 6).

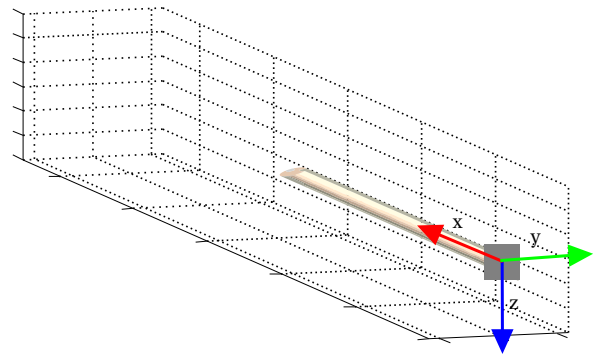


Fig. 5. Frame convention used in needle shape reconstruction

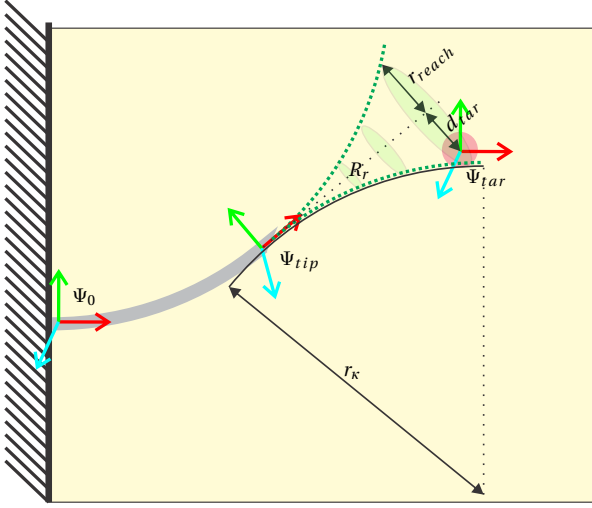


Fig. 6. Needle control frames: world frame (Ψ_0), tip frame (Ψ_{tip}) and target frame (Ψ_{tar}). Also shown is the reachable area (R_r) at several distances x . At the target location, the radius (r_{reach}) describing the reachable area and the target distance (d_{tar}) from the center of the reachable area are shown.

The needle used in our research has a limited amount of FBG sensors. This limits the complexity of the needle shape that can be reconstructed, and thus the amount of bends the shape can consist of. The controller developed in this study minimizes the amount of bends by checking whether the target is reachable when continuing at the current needle rotation angle (Fig. 7). If this is not the case, the algorithm determines the optimal rotation angle to get the shortest path to the target and rotates the needle accordingly.

The algorithm consists of four parts. First of all homogeneous matrices (\mathbf{H}_{tar}^0 , \mathbf{H}_{tip}^0) are constructed, that relate the frames at the needle-tip (Ψ_{tip}) and target (Ψ_{tar}) to a world-frame (Ψ_0) (Fig. 6) according to

$$\mathbf{H}_{tar}^0 = \begin{bmatrix} 1 & 0 & 0 & \mathbf{P}_{tar}^0 \\ 0 & 1 & 0 & \\ 0 & 0 & 1 & \\ 0 & 0 & 0 & 1 \end{bmatrix} \quad (6)$$

$$\mathbf{H}_{tip}^0 = \begin{bmatrix} \mathbf{R}_{tip}^0(0, \beta, \gamma) & \mathbf{P}_{tip}^0 \\ 0 & 0 & 0 & 1 \end{bmatrix} \quad (7)$$

Second, the target is expressed in the needle tip frame according to

$$\mathbf{H}_{tar}^{tip} = (\mathbf{H}_{tip}^0)^{-1} \cdot \mathbf{H}_{tar}^0 = \begin{bmatrix} \mathbf{R}_{tar}^{tip} & x_{tar}^{tip} \\ & y_{tar}^{tip} \\ & z_{tar}^{tip} \\ 0 & 0 & 0 & 1 \end{bmatrix}. \quad (8)$$

Next, the control law checks if the target is still within the safely reachable region (r_{safe}) defined by

$$r_{safe} = r_{reach}(x_{tar}^{tip}) \cdot K \quad (9)$$

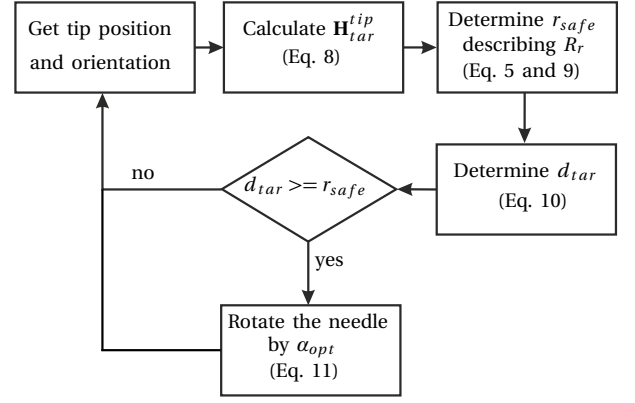


Fig. 7. Flow chart of the needle steering controller. At the start of an insertion, the needle is rotated by α_{opt} , the loop is then repeated at a set interval space during the insertion.

in which a safety margin K is taken into account for r_{reach} , to make sure the target at distance x_{tar}^{tip} stays reachable if the expected curvature was overestimated. The distance of the target to the center of the reachable region is calculated according to

$$d_{tar} = \sqrt{(y_{tar}^{tip})^2 + (z_{tar}^{tip})^2}. \quad (10)$$

Algorithm 1 Decision making algorithm

```

if ( $d_{tar} \geq r_{safe}$ )
    rotate ( $\alpha_{opt}$ );
end

```

Finally, the controller determines if it needs to rotate to keep the target in the reachable region (Alg. 1). If rotation is necessary, the needle is rotated according to the optimal rotation angle (α_{opt}) which is calculated according to

$$\alpha_{opt} = \arctan\left(\frac{z_{tar}^{tip}}{y_{tar}^{tip}}\right). \quad (11)$$

III. SETUP AND SOFTWARE

In this section, the setup used to insert the needle in gelatin phantoms is described. Section III-A describes the FBG needle and experimental setup to insert the needle into a gelatin phantom and verify the reconstructed needle shape. The camera reference is described in Section III-B.

A. Experimental setup

A setup capable of translation and rotation of the needle is used for needle steering (Fig. 8). This setup consists of a translational stage on which a rotational motor is mounted. The flexible Nitinol needle is mounted on the axis of this rotational motor using a 3D-printed holder. The needle has a total length of 185 mm, a maximum insertion length of 150 mm and a diameter of 1 mm.

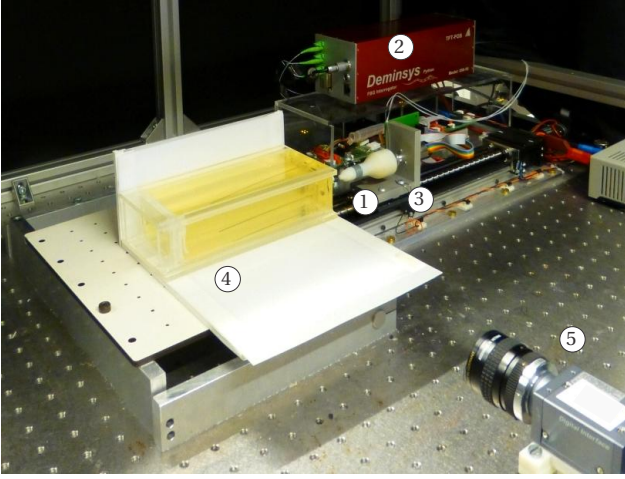


Fig. 8. Overview of the experimental setup containing the fiber Bragg grating (FBG) needle with three-dimensional (3D) printed holder (1) which is monitored by the FBG interrogator (2) and inserted by the linear stage (3) into a gelatin phantom (4) positioned on a backlight. A 3D camera system consisting of a side camera (5) and top camera (not shown) is used for reference measurements.

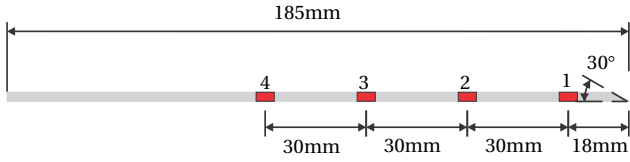


Fig. 9. Schematic representation of needle with fiber Bragg grating locations (1,2,3,4) and bevel angle

FBG sensors are placed at four locations along each of three fibers that are mounted at mutual angles of 120° in the needle shaft (Fig. 9). In this way, three FBG sensors are placed at mutual 120° angles (Fig. 10) at each location. This allows us to measure the magnitude and direction of the bending strain (Eq. 2).

The locations and rotations of the sensors on the flexible needle have been calibrated earlier by Kemp *et al.* [9] (Tab. I and II). However, in that study calibration of the hysteresis was performed for free-space rotations [9]. Because friction forces are expected to be different during a gelatin insertion, the hysteresis calibration [9] is repeated for a set of 120 mm insertions and $30^\circ/s$ rotations in a 15% gelatin phantom (15% gelatin, 85% water) (Fig. 11). The hysteresis was calibrated for the four sensor locations along the needle (Tab. II).

Table I

CALIBRATED SENSOR LOCATIONS FROM THE CENTER OF THE NEEDLE (d) WITH STANDARD DEVIATIONS (σ) AND DISTANCES d_{tip} FROM THE TIP OF THE NEEDLE

fiber	1	2	3	
loc.	$d\{\text{mm}\}$	$d\{\text{mm}\}$	$d\{\text{mm}\}$	$d_{tip}\{\text{mm}\}$
1	0.38($\sigma=0.06$)	0.31($\sigma=0.08$)	0.30($\sigma=0.06$)	18
2	0.36($\sigma=0.03$)	0.29($\sigma=0.03$)	0.31($\sigma=0.03$)	48
3	0.39($\sigma=0.02$)	0.30($\sigma=0.03$)	0.29($\sigma=0.02$)	78
4	0.35($\sigma=0.02$)	0.31($\sigma=0.02$)	0.26($\sigma=0.01$)	108

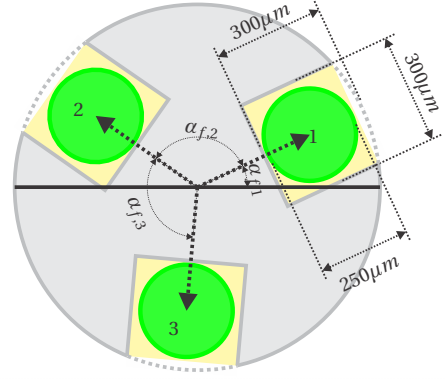


Fig. 10. Cross section ($1000 \mu\text{m}$ diameter) of the fiber Bragg grating needle with three embedded $250 \mu\text{m}$ diameter fibers in $300 \mu\text{m}$ deep and $300 \mu\text{m}$ wide grooves. The angles of the fibers with respect to each other ($\alpha_{f,i}$) are shown, where the angle for fiber 1 ($\alpha_{f,1}$) is defined with respect to the xy plane when the needle is not rotated.

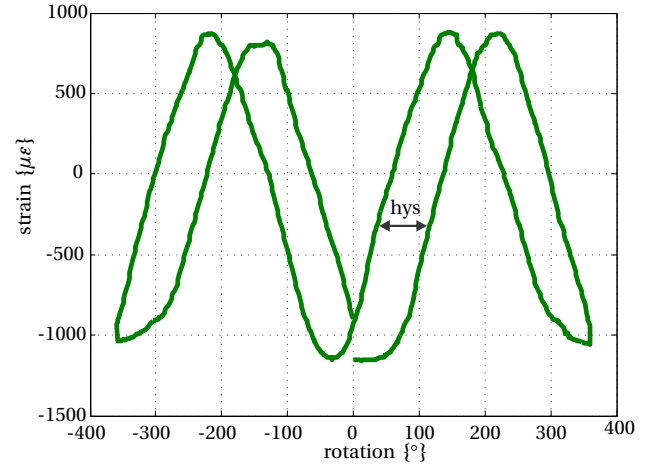


Fig. 11. Strain measurements for sensor 2 at location 2, illustrating hysteresis (hys) when rotating for a full positive and negative rotation and back to the original rotation at $30^\circ/s$.

To control needle insertion in real-time, a multithreaded C++ program is developed around the five major tasks it needs to perform (Appendix II):

- User I/O via main program loop
- Input communication with the FBG interrogator
- Needle shape calculation
- Control the insertion stage
- Needle steering control

Table II

CALIBRATED SENSOR ROTATIONS ($\alpha_{f,i}$) (FIG. 10) AND AVERAGE HYSTERESIS (α_{hys}) WITH STANDARD DEVIATION (σ) PER SENSOR LOCATION

fiber	1	2	3	
loc.	$\alpha_{f,1}\{\circ\}$	$\alpha_{f,2}\{\circ\}$	$\alpha_{f,3}\{\circ\}$	$\alpha_{hys}\{\circ\}$
1	324($\sigma=7$)	110($\sigma=14$)	124($\sigma=12$)	74($\sigma=6$)
2	320($\sigma=2$)	119($\sigma=1$)	122($\sigma=3$)	70($\sigma=7$)
3	315($\sigma=4$)	124($\sigma=1$)	118($\sigma=2$)	62($\sigma=9$)
4	312($\sigma=5$)	126($\sigma=14$)	114($\sigma=1$)	51($\sigma=7$)

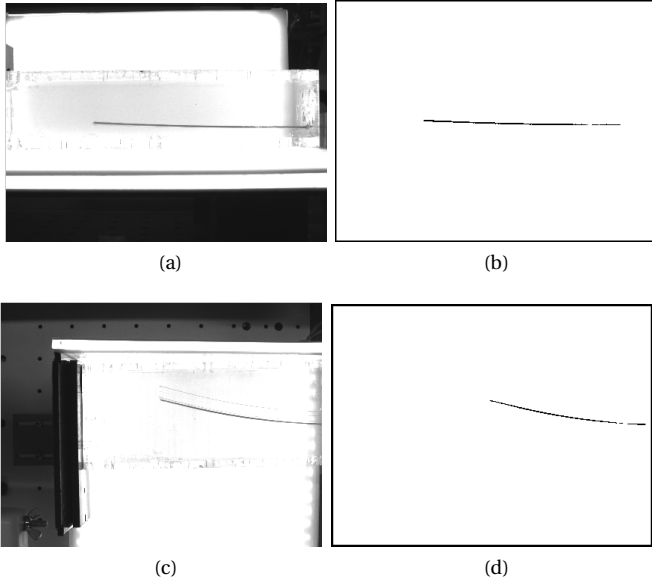


Fig. 12. Camera pixel are extracted from the raw side (a & b) and top (c & d) camera images using thresholding. The raw camera image (a & c) and the extracted needle pixels (b & d) are shown for a single bend in-plane insertion.

B. Stereo camera reference

To be able to verify the shape reconstruction of the FBG needle in gelatin, a stereo camera reference measurement is used to determine the needle shape (Appendix III). Needle shape is reconstructed by extracting the pixels belonging to the needle from the two raw 2D camera images using thresholding (Fig. 12).

In order to determine the 3D position of a pixel, a matching pixel needs to be selected in the two camera images. Matching pixel values are selected by fitting two polynomials to the two pixel sets. Sample pixels are taken at constant pixel intervals on the segments of the polynomials describing the needle. The resulting sets of samples of the two camera images were assumed to match the 3D needle shape (Fig. 13).

Using the 3D stereoscopic reconstruction described by Jahya *et al.* [19], the 3D positions of the matching pixels can be determined by undistorting them and using the pinhole descriptions of the used cameras and the homogeneous transformation matrix between the two 2D cameras (Appendix IV). The result is an array of 3D positions describing the shape of the needle (Fig. 14).

IV. RESULTS

Section IV-A discusses the results of needle shape reconstruction in gelatin using FBG sensors. Section IV-B shows how accurate the needle can be steered by combining this reconstruction with the needle steering algorithm. For all these experiments, the FBG needle with 30° bevel tip is used. As a phantom, 15% gelatin phantoms (15% gelatin, 85% water) are used at room temperature.

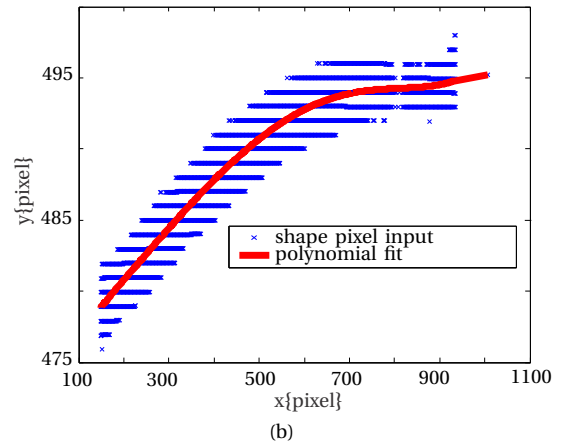
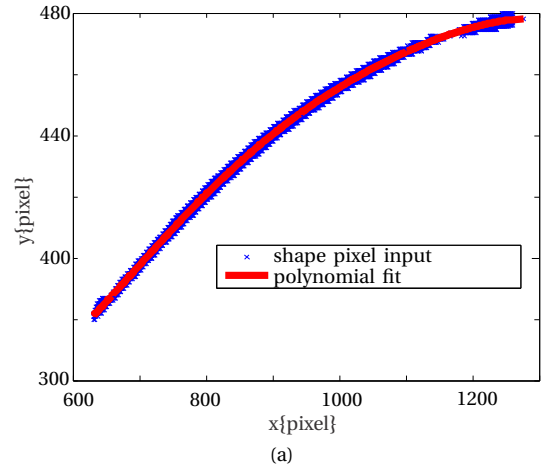


Fig. 13. Matching pixels are extracted for the total needle shape of a single bend insertion from the top (a) and side (b) cameras using polynomial fittings.

A. FBG needle shape reconstruction in gelatin

FBG needle shape is reconstructed for several types of 110-120 mm needle insertions at 10 mm/s:

- Single bend (SB) insertions, with no rotation during the insertion
- Double bend (DB) insertions, with a 180° rotation during the insertion at either 40 mm, 60 mm or 80 mm insertion length.
- 3D double bend (3DB) insertions, with a 90° rotation during the insertion at either 40 mm, 60 mm or 80 mm insertion length.
- Drilling insertions (DRILLB), with a drilling motion for the first 40 mm, 60 mm or full 120 mm insertion and an in plane single bend insertion after the drilling motion.

Because tissue characteristics will vary in practice, the exact shape of the hysteresis-loop can not be predicted. Therefore, the needle was forced into maximal (known) torsion by rotating it a full 360° left, right and back to the original rotation at 30°/s. During this rotation, the torsion can be compensated and by taking samples every 15° the average needle shape is reconstructed. Fig. 15 shows reconstruction examples for each of the four types of insertion. To verify the FBG needle shape reconstruction, the final needle shape is also reconstructed using camera images.

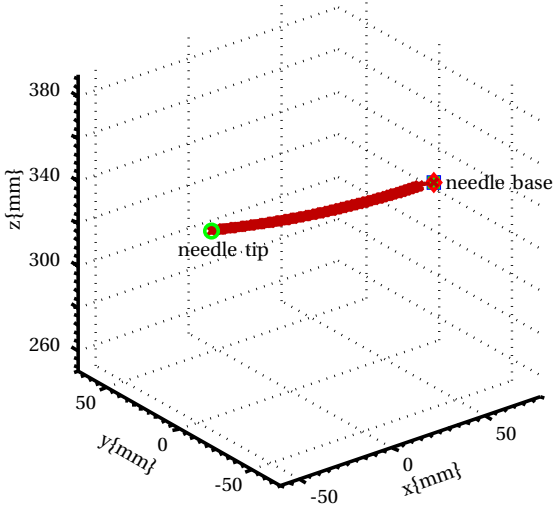


Fig. 14. Three-dimensional reconstructed needle shape from camera images for a single bend needle insertion of 120 mm at 10 mm/s into a 15% gelatin (15% gelatin, 85% water) phantom.

Resulting tip position accuracies (Tab. III) are calculated by determining the tip error (ϵ_{tip}) between the FBG-based position estimate (\mathbf{P}_{FBG}) and the camera-based position estimate (\mathbf{P}_{cam}) according to

$$\epsilon_{tip} = \|\mathbf{P}_{FBG} - \mathbf{P}_{cam}\| \quad (12)$$

and the spread of the reconstruction (spr) according to

$$spr = \sigma(\mathbf{P}_{FBG} - \mathbf{P}_{cam}). \quad (13)$$

B. Needle control using FBG feedback

Using the FBG needle shape feedback combined with the control algorithm described in Section II-B, the needle was steered to a target location. Several different 3D target locations are defined in the controller (Fig. 16).

In the first set of experiments, needle shape feedback is obtained directly from the real-time needle shape reconstruction (direct real-time control) which gives a fast (100 Hz, Appendix V), but inaccurate, shape measurement. For a second set of experiments, the average needle shape is obtained as described in Section IV-A (averaging real-time control), which results in a slower insertion, but provides more accurate shape measurements to the

Table III

RECONSTRUCTION ACCURACIES IN GEL SHOWING THE AVERAGE TIP ERROR $\mu(\epsilon_{tip})$, TIP ERROR STANDARD DEVIATION $\sigma(\epsilon_{tip})$ AND MIN./MAX. SPREAD $min(spr)$ AND $max(spr)$ FOR SEVERAL TYPES OF INSERTION. AT LEAST SIX EXPERIMENTS WERE USED TO CALCULATE EACH ACCURACY.

	$\mu(\epsilon_{tip})$	$\sigma(\epsilon_{tip})$	$min(spr)$	$max(spr)$
SB	1.5{mm}	0.8{mm}	1.2{mm}	1.8{mm}
DB	2.0{mm}	0.7{mm}	2.3{mm}	5.0{mm}
3DB	2.1{mm}	1.1{mm}	2.5{mm}	4.8{mm}
DRILLB	1.7{mm}	1.2{mm}	1.0{mm}	1.4{mm}

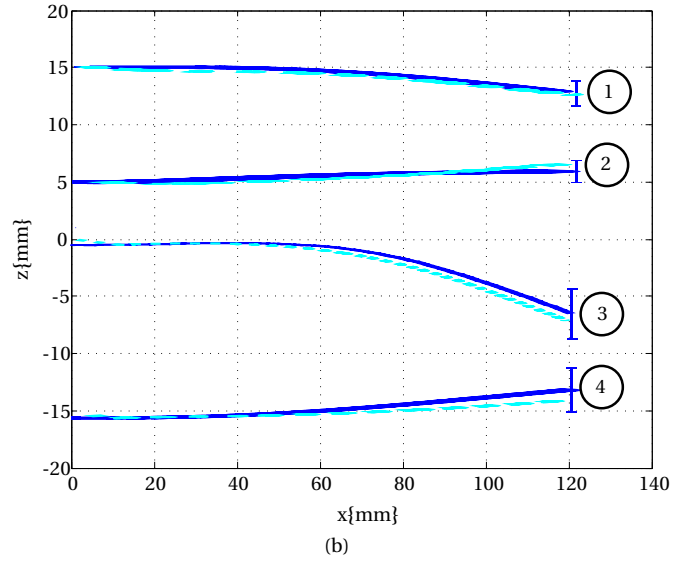
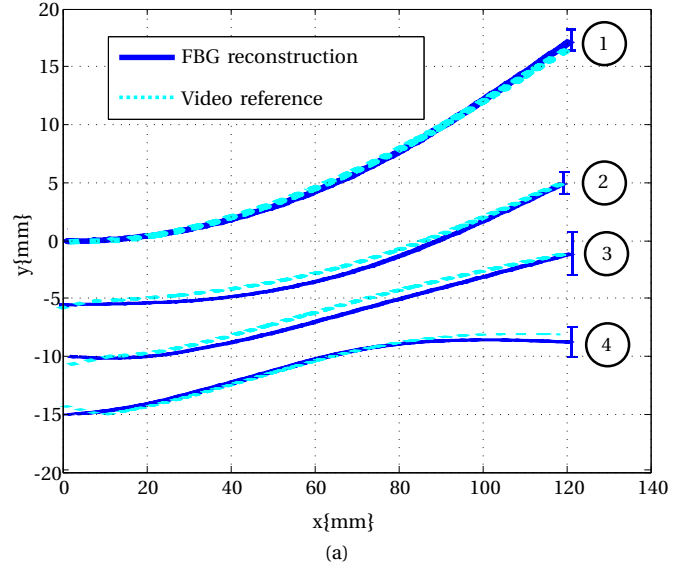


Fig. 15. Needle shape reconstruction (top view (a), side view (b)) examples in gelatin for the four types of insertion: single bend ①, drilling insertion ②, three-dimensional double bend ③ and double bend ④. Error bars at the tip reconstruction are sized according to spr (Eq. 13).

needle steering controller. The controller is set up in such a way that it makes a control decision at every 15 mm interval during the insertion. Increasing the length of this interval in some cases causes the needle to rotate too late and miss the target. Decreasing the length of the interval causes the insertion to resemble a drilling motion during averaging real-time control, thereby reducing the deflection. For direct real-time control, torsion cancels out during a translational movement of the needle after rotation. Decreasing the interval length would thus increase hysteresis errors when using direct real-time control. The experiment is repeated three times for each target location for both direct and averaging real-time control. Reconstructed needle shapes are shown for the different targets in Fig. 17.

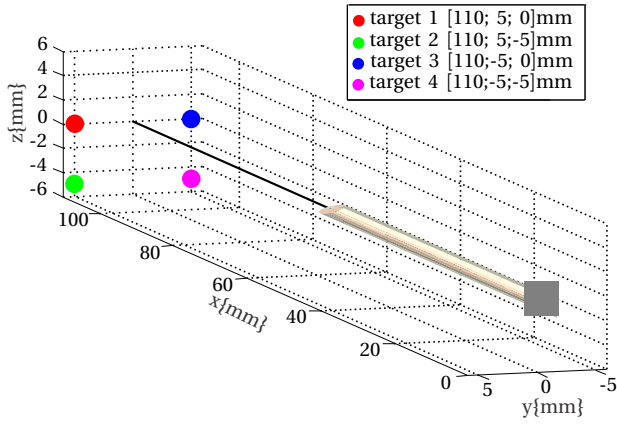


Fig. 16. Illustration of the needle (1) and the control target locations (2)

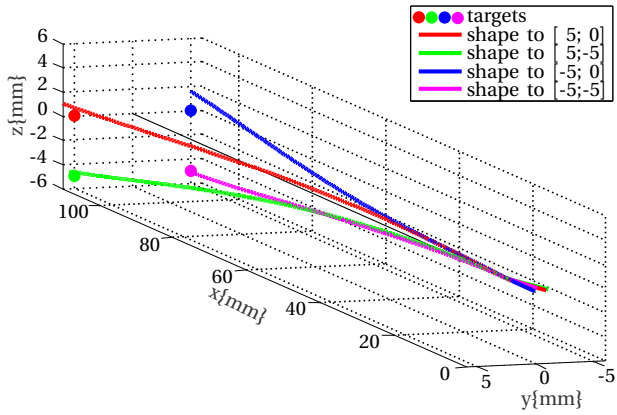


Fig. 17. Needle shape results for the different targets from the camera reference. One reconstruction from an averaging real-time control experiment is shown for each target.

Reconstruction accuracies for the two control methods are shown in Tab. IV in which the targeting error (ϵ_{tip}) is defined according to

$$\epsilon_{tip} = \left\| \mathbf{P}_{tip}^0 - \mathbf{P}_{tar}^0 \right\| \quad (14)$$

Results show that the average targeting error ($\mu(\epsilon_{tip})$) is 1.2 mm according to the FBG sensors. According to the camera reference, the average targeting error is 1.3 mm.

V. CONCLUSIONS AND RECOMMENDATIONS

This study has shown that needle shape reconstruction using FBG sensors is a promising technique to steer needles in tissue. Needle shape reconstruction accuracies in gelatin

Table IV
NEEDLE STEERING ACCURACIES SHOWING AVERAGE TARGETING ERROR ($\mu(\epsilon_{tip})$) AND STANDARD DEVIATION ($\sigma(\epsilon_{tip})$) FOR THE ACHIEVED POSITION (CAMERA) AND PERCEIVED POSITION (FBG)

Control type	FBG		Camera	
	$\mu(\epsilon_{tip})$	$\sigma(\epsilon_{tip})$	$\mu(\epsilon_{tip})$	$\sigma(\epsilon_{tip})$
averaging real-time	1.2{mm}	0.5{mm}	1.3{mm}	0.9{mm}
direct real-time	2.6{mm}	0.9{mm}	3.9{mm}	0.5{mm}

tissue phantoms vary with needle shape and range from 1.5 mm for single bend insertions to 2.1 mm for 3D double bend insertions. A controller has been developed that uses FBG needle shape feedback for needle steering. Using this controller, target locations are reached in 3D with an average targeting error of 1.3 mm.

This study illustrates that a different needle design can improve the accuracy of the needle shape reconstruction. A smoother needle with less torsional compliance would show less hysteresis when rotating the needle. The hysteresis effects in gelatin phantoms are large and the hysteresis calibration only holds for a specific type of gel at room temperature. Also, adding a sensor located closer to the base of the needle would increase the maximum insertion length. More accurately fabricated needles, in particular with more accurate sensor locations, would show less uncertainty on the reconstructed needle tip position.

An improved needle design would be similar to a standard biopsy needle, in which the FBG sensors are embedded inside the needle. A smooth intact outer sleeve would make the needle more torsion stiff, whilst also reducing friction. Adding extra FBG sensors to each of the three fibers along the needle would also increase accuracy and enable accurate shape reconstruction for needle shapes with more than two bends. Furthermore, distribution of the sensors over the length of the needle is important. Curvatures at the base of the needle influence the deflection of the entire needle while curvatures near the tip only influence the deflection of the part up to the tip. Distributing the sensors so that the concentration of sensors is higher at the base of the needle would increase accuracy.

Needle shape reconstruction using FBG sensors shows to be a promising technique. A needle that can obtain larger deflections would enable an interesting combination of FBG needle shape reconstruction with algorithms for path planning and obstacle avoidance.

ACKNOWLEDGEMENTS

The authors are affiliated with MIRA - Institute for Biomedical Technology and Technical Medicine, University of Twente, the Netherlands. This work is supported by funds from the Netherlands Organization for Scientific Research (NWO).

REFERENCES

- [1] N. Abolhassani, R. Patel, and M. Moallem, "Needle insertion into soft tissue: A survey," *Medical Engineering & Physics*, vol. 29, no. 4, pp. 413 – 431, 2007.
- [2] S. Patil and R. Alterovitz, "Interactive motion planning for steerable needles in 3d environments with obstacles," in *proceeding of the IEEE RAS and EMBS International Conference on Biomedical Robotics and Biomechatronics (BioRob)*, pp. 893 – 899, Tokyo, Japan, September 2010.
- [3] P. M. Novotny, J. A. Stoll, N. V. Vasilyev, P. J. del Nido, P. E. Dupont, T. E. Zickler, and R. D. Howe, "Gpu based real-time instrument tracking with three-dimensional ultrasound," *Medical Image Analysis*, vol. 11, no. 5, pp. 458 – 464, 2007.
- [4] S. DiMaio, E. Samset, G. Fischer, I. Iordachita, G. Fichtinger, F. Jolesz, and C. Tempany, "Dynamic mri scan plane control for passive tracking of instruments and devices," in *Medical Image Computing and Computer-Assisted Intervention*, pp. 50–58, Springer Berlin / Heidelberg, 2007.

- [5] H. Fred, "Drawbacks and limitations of computed tomography," *Texas Heart Institute Journal*, vol. 31, no. 2, pp. 345–348, 2004.
- [6] A. Othonos, K. Kalli, D. Pureur, and A. Mugnier, "Fibre bragg gratings," in *Wavelength Filters in Fibre Optics*, pp. 189–269, Springer Berlin / Heidelberg, 2006.
- [7] Y.-L. Park, S. Elayaperumal, B. Daniel, C. R. Seok, S. Mihye, J. Savall, R. Black, B. Moslehi, and M. Cutkosky, "Real-time estimation of 3-d needle shape and deflection for mri-guided interventions," *IEEE/ASME Transactions on Mechatronics*, vol. 15, no. 6, pp. 906 – 915, 2010.
- [8] K. Henken, D. Van Gerwen, J. Dankelman, and J. Van Den Dobbelsteen, "Accuracy of needle position measurements using fiber bragg gratings," *Minimally Invasive Therapy & Allied Technologies*, vol. 0, no. 0, pp. 1–7, 2012.
- [9] M. Kemp, M. Abayazid, R. J. Roesthuis, and S. Misra, "Flexible needle steering using fiber bragg grating sensors," Master's thesis, Part I: "Calibration and Shape Reconstruction of a Flexible Needle using Fiber Bragg Grating Sensors", University of Twente, August 2012.
- [10] V. Kallem and N. Cowan, "Image-guided control of flexible bevel-tip needles," in *proceedings of the IEEE International Conference on Robotics and Automation (ICRA)*, pp. 3015 –3020, Rome, Italy, April 2007.
- [11] D. Glozman and M. Shoham, "Flexible needle steering and optimal trajectory planning for percutaneous therapies," in *Medical Image Computing and Computer-Assisted Intervention*, pp. 137–144, Springer Berlin / Heidelberg, 2004.
- [12] D. Glozman and M. Shoham, "Image-guided robotic flexible needle steering," *IEEE Transactions on Robotics*, vol. 23, no. 3, pp. 459 –467, 2007.
- [13] K. Reed, V. Kallem, R. Alterovitz, K. Goldbergx, A. Okamura, and N. Cowan, "Integrated planning and image-guided control for planar needle steering," in *proceeding of the IEEE RAS and EMBS International Conference on Biomedical Robotics and Biomechanics (BioRob)*, pp. 819 –824, Scottsdale, USA, October 2008.
- [14] J. van den Berg, S. Patil, R. Alterovitz, P. Abbeel, and K. Goldberg, "Lqg-based planning, sensing, and control of steerable needles," in *Algorithmic Foundations of Robotics IX*, pp. 373–389, Springer Berlin / Heidelberg, 2011.
- [15] C. M. Schneider, "Systems for robotic needle insertion and tool-tissue interaction modeling," Master's thesis, The Johns Hopkins University, 2004.
- [16] T. Megson, *Structural and Stress Analysis*. Butterworth-Heinemann, 2005.
- [17] S. Misra, K. Reed, B. Schafer, K. Ramesh, and A. Okamura, "Mechanics of flexible needles robotically steered through soft tissue," *The International Journal of Robotics Research*, vol. 29, no. 13, pp. 1640–1660, 2010.
- [18] R. J. Webster, J. S. Kim, N. J. Cowan, G. S. Chirikjian, and A. M. Okamura, "Nonholonomic modeling of needle steering," *The International Journal of Robotics Research*, vol. 25, no. 5-6, pp. 509–525, 2006.
- [19] A. Jahya, F. van der Heijden, and S. Misra, "Observations of three-dimensional needle deflection during insertion into soft tissue," in *proceedings of the IEEE RAS/EMBS International Conference on Biomedical Robotics and Biomechanics (BioRob)*, Rome, Italy, June 2012.

Discussion

Flexible needles with asymmetric beveled tips can be used for clinical procedures (e.g., biopsy, brachytherapy). Robotically steering such needles relies on needle shape feedback, which up to now has been provided by clinical imaging modalities. Unfortunately, clinical imaging modalities have several drawbacks for real-time applications such as low refresh rates (magnetic resonance images), low spatial accuracy (ultrasound images) and high radiation exposure (computed tomography scans). One solution is to use fiber Bragg grating (FBG) sensors to reconstruct needle shape.

In this study, twelve FBG sensors were embedded in a 1.0 mm diameter flexible Nitinol needle. Using these sensors, bending strain was measured at several locations along the needle shaft. Three-dimensional (3D) needle curvature was determined from these strain measurements. A nearest neighbor interpolation was used to estimate the curvature along the entire needle. By integrating the resulting curvature function, 3D needle shape was obtained.

Uncertainties in sensor position and orientation limited the accuracy of the needle shape reconstruction. Besides this, hysteresis effects were noticed during rotations. A calibration method was described to determine sensor locations and orientations and hysteresis due to torsion in the needle. This calibration allowed us to compensate for sensor placement and hysteresis effects.

Shape reconstruction has been shown in 3D for free-space experiments with an average 3D tip-error of 0.9 mm for single bend deflections. Two-dimensional (2D) and 3D double bend deflections showed average 3D tip-errors of 1.0 mm and 1.4 mm, respectively.

Needle shape was also reconstructed in real-time for both in-plane and out-of-plane needle insertions in gelatin phantoms. A stereo camera system provided a reference measurement of the needle shape. Reconstructed needle shapes showed an average 3D tip-error of 1.5 mm for single bend insertions, 2.0 mm for in-plane double bend insertions and 2.1 mm for out-of-plane double bend insertions.

Finally, a 3D needle steering controller was developed based on the kinematics-based unicycle model. By combining this controller with real-time FBG needle shape feedback, the needle was steered towards a 3D target location. The average targeting error was 1.3 mm.

Conclusions

Previous studies have reconstructed needle shape for 2D free-space deflections. This research showed that FBG sensors can be used to reconstruct needle shape for both 3D free-space deflections and needle insertions in soft tissue phantoms. This was experimentally validated in free-space and gelatin phantoms resulting in average 3D tip-errors of 0.9-1.4 mm and 1.5-2.1 mm, respectively. We determined that the shape reconstruction accuracy is influenced by the needle design and accuracy of the sensor placement. Shape reconstruction accuracy was increased by calibrating sensor locations and needle hysteresis. Moreover we have shown that needle steering can be done using FBG-based needle shape feedback. Target locations could be reached in 3D with an average targeting error of 1.3 mm. These results show that FBG sensors provide a viable alternative to imaging modalities when it comes to providing real-time needle shape feedback.

Future work

The current study showed the potential of FBG sensors for shape reconstruction, but also highlighted design errors in the used FBG needle. A possible alternative to the current needle design would be a design similar to a standard biopsy needle, in which the outer needle is kept intact and the FBG sensors are embedded in the inner needle. This design is torsionally stiff and thus reduces hysteresis-effects. Uncertainties in sensor positions could be reduced by using a single multi-core fiber instead of three single-core fibers. As the distance between the different cores of the multi-core fiber is accurately known this would increase sensor position accuracy. Finally, more sensors should be placed closer to the needle base, which would increase shape reconstruction accuracy.

The needle used in this study has a 1.0 mm diameter, which limited deflection. By using a needle with a smaller diameter, higher deflections could be obtained. This would open the door to new research combining FBG needle shape reconstruction with algorithms for path planning, target tracking and obstacle avoidance. Experiments in biological tissue, in which path planning is performed based on target tracking data and real-time FBG needle shape reconstruction, will allow us to come closer to real-life applications.

Appendices

Appendix I: extra experiments

During the course of this study, several experiments were performed which are not mentioned in Part I and Part II of this thesis. Some of these experiments did bring interesting experiments to light. A short overview of these experiments is shown in this Appendix.

Fixed curvature sensor calibration and torsional compliance

During the first stages of this study, fixed curvature grooves were etched into a plexiglass plate (Fig. 1). During measurements where the needle was placed in these grooves, the torsional compliance of the needle was noticed. Hysteresis effects were unfortunately too large to do an accurate calibration using this plate, as the friction in the grooves was very high and not constant during the rotation.

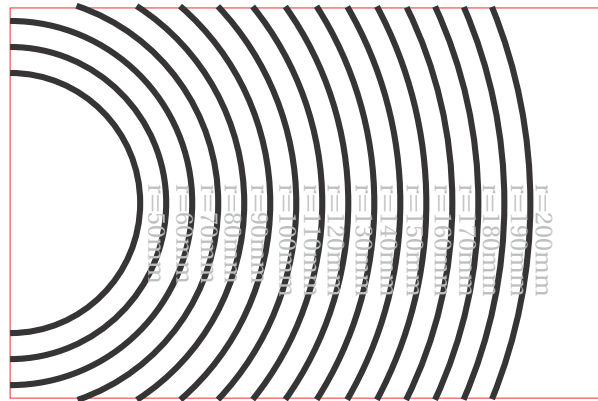


Fig. 1: Plexiglass plate design showing fixed curvature grooves for several radii of curvature

Free-space double bend experiments with different plate locations

During the course of this study, free-space experiments were performed for different plate locations. The plates were positioned at 53 mm and 124 mm instead of 75 mm and 109 mm as used in part I of this thesis. The results showed to be less accurate. The FBG sensors were located too far from the needle base and therefore curvature was not accurately estimated near the needle base. As the curvature near the base has an effect on the shape of the entire needle, accuracies decreased. The difference in the accuracies shown in Tab. 1 illustrates that it is essential to have an accurate curvature measurement near the needle base. The error (ϵ_{tip}) and spread (σ_{spr}) are defined in Eq. 22 and 23 in part I of this thesis.

Shape	Method	$\mu(\epsilon_{tip})$	$\sigma(\epsilon_{tip})$	$min:max(\sigma_{spr})$
DB 1	NN	0.9	0.5	1.0 : 2.1
	PCHIP	1.0	0.5	1.0 : 2.1
DB 2	NN	4.4	1.9	0.7 : 1.5
	PCHIP	4.6	2.0	0.7 : 1.5

Table 1: Comparison of double bend accuracies in free-space for different plate locations. DB 1 shows the accuracies obtained with plates at 75 mm and 109 mm, for which a needle insertion of ~110 mm was used. DB 2 shows the accuracies obtained with plates at 53 mm and 124 mm, for which a needle insertion of ~125 mm was used.

Appendix II: C++ code

Several parts of C(++)-code were written for this study, all contained in one program. The main of this program starts all hardware and provides I/O with the user: the user can choose for manual control of the Insertion Stage or have the designed controlled steer the needle to a preset target. The next subsections give a short overview of the major blocks of code that are used in the program.

Communication with the FBG interrogator

The FBG processing code is contained within a separate thread which runs *pcap_testlooper(inum)*. This piece of code starts up the network interface and calls *packet_handler()* each time a UDP packet is received from the interrogator. The function *packet_handler()* reads the FBG data values from the received packet and applies the calibration to calculate the strains measured by each sensor. The strains are also scaled in this function so the output strains all seem to be measured at 0.35 mm distance from the needle heartline.

Needle shape calculation

Needle shape calculation is done in a separate thread running *Shape_calculator(NeedleInsDev* NID)*. This thread loops and uses the current FBG values and Insertion Device encoder. First of all the 3D curvature is calculated at each sensor location using *straincalculator->calculate()*. Next the curvatures are interpolated using *Interpolation_calculator(e_max, a, encoder_values, #samples)*. Last the Curvature is integrated using *Shape_integrator(#samples)*. *#samples* is used to set the number of steps the interpolation and integration use to sample and integrate. The result is an array of 3D points: *Curvature_positions[#samples]* (x), *Shape_integrated_y[#samples]* (y) and *Shape_integrated_z[#samples]* (z).

Needle steering / control

Control of the hardware is done using a software package by Guus Vroojink. This package communicates to the Elmo motor controllers via CAN-bus. It allows the user to use the motors in position control.

The controller action is determined by the function

`opt_angle = steeringAlgorithm(NID, X_tip, Y_tip, Z_tip, X_tar, Y_tar, Z_tar, phi_slopeZ, phi_slopeY)`

which determines if the needle needs to rotate according to the current needle tip position (X_tip, Y_tip, Z_tip) and direction (phi_slopeZ, phi_slopeY) and target position (X_tar, Y_tar, Z_tar). The controller calculations are described in Paper II.

Appendix III: Matlab and excel code

Several pieces of MATLAB code have been created to process experimental data:

- a set of functions to offline process FBG data to needle shape. Contained in "FBG_total_system". The main.m script runs all needed steps automatically if parameters are set correctly.
- a set of function to process camera images to needle shape. Contained in "camera_reference". One can use the reconstruction_3D_shape.m script which automatically has the user set correct parameters. For extra dark or light images, thresholds might need to be changed in this script.
- a set of functions to calculate the theoretical fitting and errors in the resulting shapes. Contained in "theoretical_best_fitting". The script main.m runs all used functions automatically if the correct parameters are set.
- a set of calibration functions which automatically calculates sensor locations, rotations and hysteresis when correct FBG input is given and parameters are set correctly. All contained in "calibration". Running full_calibration_routine.m with correctly set parameters will run all used functions and give calibration values for the input experiment automatically.

Appendix IV: Camera shape reconstruction

For the 3D needle shape reconstruction from camera images, the camera focal lengths ($\mathbf{f}_{c,cam}$), camera centers ($\mathbf{C}_{c,cam}$), distortion ($\mathbf{k}_{c,cam}$) and the homogeneous matrix between the top and side camera (\mathbf{H}_{top}^{side}). The values for these parameters were calculated using the Matlab Camera Calibration Toolbox. The used values for these calibrated parameters were:

$$\mathbf{f}_{c,side} = [2285.1164 \quad 2279.8028]$$

$$\mathbf{f}_{c,top} = [3286.1293 \quad 3269.0216]$$

$$\mathbf{C}_{c,side} = [641.1685 \quad 465.7420]$$

$$\mathbf{C}_{c,top} = [657.5472 \quad 583.6790]$$

$$\mathbf{k}_{c,side} = [-0.2207 \quad 0.1964 \quad -0.0004 \quad -0.0002 \quad 0]$$

$$\mathbf{k}_{c,top} = [-0.3668 \quad -1.2971 \quad -0.0014 \quad 0.0003 \quad 19.1933]$$

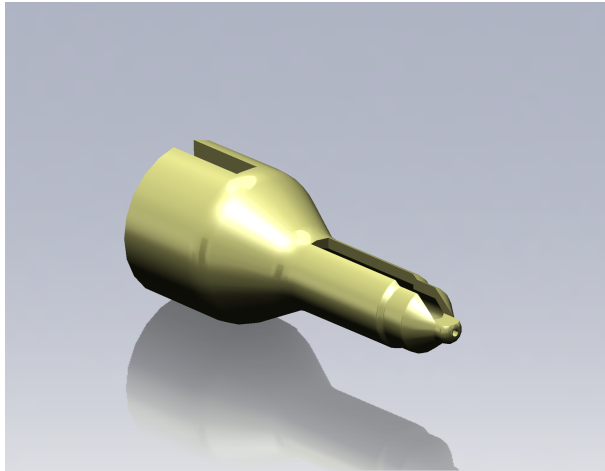
$$\mathbf{H}_{top}^{side} = \begin{bmatrix} 0.9998 & 0.0151 & 0.0130 & 34.0700 \\ 0.0136 & -0.0408 & -0.9991 & 301.4448 \\ -0.0146 & 0.9991 & -0.0410 & 623.5388 \\ 0 & 0 & 0 & 1 \end{bmatrix}$$

Appendix V: FBG Interrogator speed

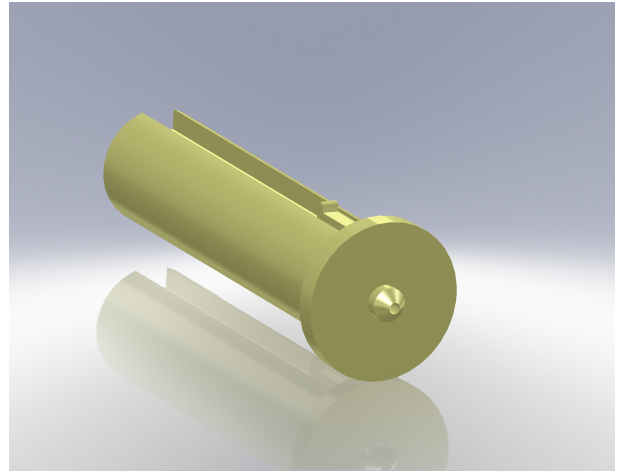
The interrogator used in this research (Deminsys Python 850-55 FBG interrogator (Technobis Fiber Technologies BV, Uitgeest, Netherlands)) has a maximum sampling speed of 20kHz. In this research, a moving average over 200 samples is used, which results in a less noisy measurement. Resulting from this, the twelve measured strain-values for the twelve FBG sensors in the used needle are outputted by the interrogator at 100Hz. The shape reconstruction thread processes this datastream in realtime and produces a shape estimate of the needle at 100Hz.

Appendix VI: CAD drawings

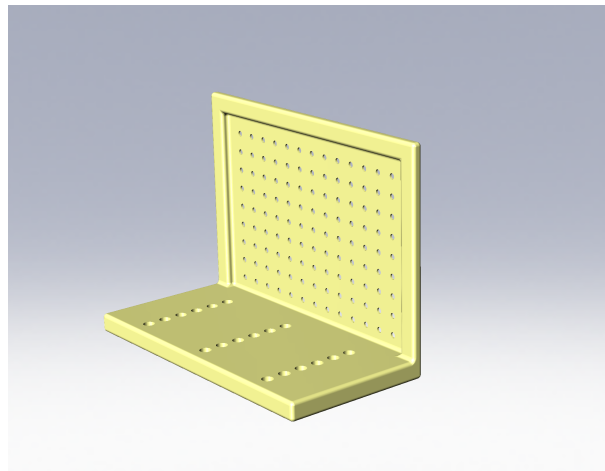
Several parts have been designed during this study. A holder for the FBG needle has been designed, to be able to mount the needle on the existing needle insertion device, a straightguide plug has been made to ensure starting angles of the FBG needle were fixed to 0° at the needle base and two plates have been designed to be able to apply free-space deflections on the needle. CAD drawings of these designs are shown in Fig. 2 to 4. The designs were manufactured using a 3D-printer.



(a) CAD drawing of the holder used to mount the FBG needle on the insertion device



(b) CAD drawing of the straightguide plug used to fix needle base angles to 0°



(c) CAD drawing of the plate used to apply free-space deflections to the needle

Fig. 2: CAD drawings of the designed parts